JGR Solid Earth

RESEARCH ARTICLE
10.1029/2021JB022878

# Time-Lapse Record of an Earthquake in the Dry Felsic Lower Continental Crust Preserved in a Pseudotachylyte-Bearing Fault

**Neil S. Mancktelow[1], Alfredo Camacho[2], and Giorgio Pennacchioni[3]**

[1]Department of Earth Sciences, ETH Zurich, Zurich, Switzerland, [2]Department of Earth Sciences, University of Manitoba, Winnipeg, MB, Canada, [3]Department of Geosciences, University of Padua, Padua, Italy

**Key Points:**

- Time sequence of microstructures related to pseudotachylyte formation in the lower continental crust (Musgrave Ranges, central Australia)
- Dry conditions with no infiltration of water-rich fluid before, during, or after seismic rupturing and pseudotachylyte development
- Asymmetric fracturing, local garnet pulverization, and high-temperature frictional melting represent different stages of a single earthquake rupture

**Supporting Information:**

Supporting Information may be found in the online version of this article.

**Correspondence to:**

G. Pennacchioni,
giorgio.pennacchioni@unipd.it

**Citation:**

Mancktelow, N. S., Camacho, A., & Pennacchioni, G. (2022). Time-lapse record of an earthquake in the dry felsic lower continental crust preserved in a pseudotachylyte-bearing fault. *Journal of Geophysical Research: Solid Earth*, *127*, e2021JB022878. https://doi.org/10.1029/2021JB022878

Received 22 JUL 2021
Accepted 12 MAR 2022

**Author Contributions:**

**Conceptualization:** Neil S. Mancktelow, Alfredo Camacho, Giorgio Pennacchioni
**Data curation:** Neil S. Mancktelow, Alfredo Camacho, Giorgio Pennacchioni
**Formal analysis:** Neil S. Mancktelow
**Funding acquisition:** Giorgio Pennacchioni
**Investigation:** Neil S. Mancktelow, Alfredo Camacho
**Methodology:** Neil S. Mancktelow
**Software:** Neil S. Mancktelow
**Writing – original draft:** Neil S. Mancktelow



**Abstract** The mechanisms of earthquake rupture in lower continental crust, below the usual frictional-viscous transition, remain uncertain. In addressing this problem, the study of pseudotachylyte (quenched frictional melt produced during seismic fault slip) and related structures from deeply exhumed rocks can provide direct observational constraints. A felsic granulite from the Musgrave Ranges (central Australia) exceptionally preserves pristine microstructures spatially related to a pseudotachylyte. This sample remained dry, without introduction of hydrous fluids, during pseudotachylyte development and subsequent exhumation. It was therefore unaffected by alteration and metamorphic re-equilibration. Fractures in the damage zone developed asymmetrically to either side of the pseudotachylyte and are marked by new, randomly oriented quartz, feldspar, and garnet grains. Pulverization of garnet occurred locally between intersecting fractures with powder injected into dilatant fractures in a quartz inclusion within the garnet host. Injection of pulverized material can explain the growth of new, compositionally different minerals (quartz, feldspar, kyanite, ilmenite, magnetite, and rutile) along dilatant fractures developed in a short-lived seismic event. The pseudotachylyte contains only clasts of quartz, suggesting an unusually high melting temperature. The sequentially developed microstructures provide a time-lapse record of thermomechanical processes during a single earthquake event, including initial rupture propagation with associated off-fault damage and local pulverization during very dynamic fluctuations in the local stress field; frictional heating and eventual melting during fault slip; flow and injection of melt; and rapid solidification (quenching) and crystallization of new minerals. This occurred under lower continental crustal conditions of ca. 650°C and 1.2 GPa about 550 Myrs ago.

**Plain Language Summary** Some special rocks (pseudotachylytes: quenched melts produced by frictional heating during seismic slip on a fault) exhumed from deep in the Earth's crust provide the opportunity to study old earthquakes that occurred at depths that are not directly observable. The pseudotachylyte we studied from the Musgrave Ranges in central Australia was formed during a single earthquake some 550 million years ago at depths of ca. 40 km and temperatures of ca. 650°C, but remained remarkably well preserved on its path to the Earth's surface. As a result, the sample preserves a complete time-lapse record of the sequence of microstructures representative of different thermal and mechanical processes, which lasted only seconds to minutes during a seismic event, including initial fracture propagation, off-fault damage with local pulverization, and development, flow, and final solidification of frictional melt.

## 1. Introduction

Earthquakes recorded in the lower continental crust present a major conundrum with regard to rock mechanics and earthquake mechanisms because they occur well below the depth of the usual frictional to viscous (or brittle to ductile) transition. The properties and mechanical processes of these lower crustal earthquakes have generally been inferred from geophysical data, from laboratory experiments, or from analytical and numerical models. Complementary information comes from the study of exhumed rocks and in particular of pseudotachylytes, which are special fault rocks widely recognized as quenched melts produced during coseismic slip in silicate rocks (e.g., Austrheim & Boundy, 1994; Bestmann et al., 2011, 2016; Di Toro et al., 2009; Maddock, 1983; Sibson & Toy, 2006). Pseudotachylytes are usually related to brittle-frictional deformation in shallow-depth (≤15 km) faults (Sibson, 1975), but have been also found in several exposures worldwide of lower crustal rocks: the Bergen Arcs, southern Norway (Austrheim, 1987; Austrheim & Griffin, 1985; Boundy et al., 1992; Petley-Ragan et al., 2018); Lofoten, northern Norway (Menegon et al., 2017; Steltenpohl et al., 2006); the Mont Mary area

**Writing – review & editing:** Neil S. Mancktelow, Alfredo Camacho, Giorgio Pennacchioni

and Ivrea Zone, northern Italy (Pittarello et al., 2012); Calabria, southern Italy (Altenberger et al., 2011, 2013); Cora Lake shear zone, western Canada (Orlandini et al., 2018; Orlandini & Mahan, 2020); and the Musgrave Ranges, central Australia (Camacho et al., 1995; Hawemann et al., 2018).

Because of the high temperature and pressure ambient conditions at intermediate to deep crustal levels, where rocks are commonly assumed to flow rather than fracture (e.g., Handy et al., 2007; Kohlstedt et al., 1995; Sibson, 1977, 1982), two main opposing models have been proposed for the origin of deep-seated pseudotachylytes (and therefore for the mechanics of the associated deep-seated deformation): (a) mechanical instability during ductile solid-state flow (thermal runaway process) or (b) purely brittle-frictional slip. In the former model, seismic slip results from the positive feedback between shear heating, viscosity, and strain rate that induces, in a localized shear zone, a progressive slip acceleration eventually leading to melting along the slip surface (John et al., 2009; Kelemen & Hirth, 2007; Papa et al., 2020; Thielmann, 2018; Thielmann et al., 2015). In contrast, the brittle-frictional slip model considers deformation processes similar to those occurring for shallow earthquakes, involving a sequence of short-lived deformations (Sibson, 1980; White, 1996) that result from (a) initial propagation of the earthquake rupture (at a speed of kilometers per second), (b) accumulation of seismic slip along the fault (at a speed of meters per second) with friction-induced thermal heating, and (c) eventually melting and pseudotachylyte production (Di Toro, Pennacchioni, & Teza, 2005; Okubo et al., 2019; Petley-Ragan et al., 2019). The brittle behavior of lower crustal granulite-facies rocks hosting pseudotachylytes has been related to water-absent conditions, making high-temperature rocks strong and metastable (Jamtveit, Ben-Zion et al., 2018; Jamtveit et al., 2019).

Studying the seismic behavior of the lower continental crust by direct observation in exhumed deep-seated pseudotachylyte-bearing rocks is not, however, an easy task. Because of the long time spent at elevated temperature and pressure, as well as the high potential for subsequent tectonic and metamorphic overprint at depth or during exhumation, pristine pseudotachylytes and associated coeval microstructures are rarely preserved in the geological record. An additional complication arises from the multiple reactivation of many seismic faults, which may obliterate features associated with a single-jerk sequence of deformational events. Furthermore, some deep-seated pseudotachylytes, for example from the classic location of the Bergen Arcs, are followed by extensive infiltration of aqueous fluids with the hydration triggering metamorphic re-equilibration and ductile flow (Austrheim, 1987; Austrheim & Engvik, 1997; Jamtveit et al., 1990, 2019; Jamtveit, Moulas, et al., 2018; Kaatz et al., 2021; Lund & Austrheim, 2003). This may also obliterate the former coseismic microstructural record.

In this study, we present observations from a sample collected in the Musgrave Ranges (central Australia), which contains exceptionally well-preserved microstructures related to formation of a single isolated vein of pseudotachylyte. We document the brittle, crystal-plastic, and melt microstructures and establish a relative chronology of microstructural development. The sequence of microstructures represents a rather unique time-lapse record of a single lower crustal earthquake that lasted seconds to minutes, hundreds of millions of years ago. Observations on the mineralogy, microstructure, and grain (or clast) size distributions provide direct constraints on proposed models for dynamic earthquake rupture at lower crustal depth.

## 2. Geological Setting and Sample Description

The Musgrave Province of central Australia is a granulite to amphibolite facies terrane with an E-W extent of ca. 700 km. Two major orogenic periods affected the area (a) the Musgravian Orogeny at ca. 1220-1150 Ma, which produced high-temperature (ca. 900°C) granulites and anhydrous syn- to post-tectonic granites, at mid-crustal pressures of ~0.6–0.8 GPa (e.g., Walsh et al., 2015), and (b) the Petermann Orogeny at ca. 630–520 Ma with peak conditions of ~600–700°C and 1.0–1.2 GPa (Camacho et al., 1997; Camacho & McDougall, 2000; Ellis & Maboko, 1992; Hawemann et al., 2018; Wex et al., 2018). The studied sample AW9 was collected from the hanging wall of the crustal-scale Woodroffe Thrust (Figure S1 in Supporting Information S1; Bell, 1979; Bell & Etheridge, 1976; Major, 1973), which had a ca. top-to-N displacement of at least 60 km during the Petermann Orogeny (Wex et al., 2017). The Woodroffe Thrust and its immediate hanging wall contain one of the largest concentrations of exhumed mid-lower crustal pseudotachylytes in the world (Camacho et al., 1995; Lin et al., 2005), which were developed during the Petermann Orogeny (Hawemann et al., 2018; Wex et al., 2017).

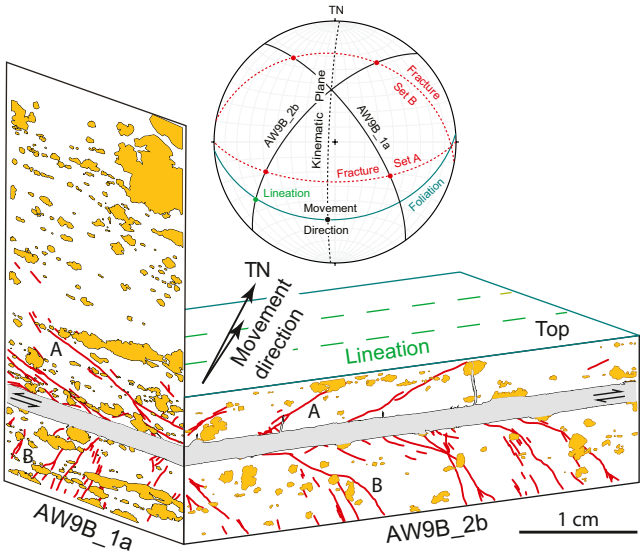


**Figure 1.** Block diagram showing the geometric relationships for the two thin sections examined in this study with garnets shaded in orange and fractures shown as red lines. The pseudotachylyte is parallel to the older granulite facies foliation (dip direction/dip: 176/36, relative to True North, TN), which carries a clear lineation (plunge direction/plunge: 234/20). Thin sections were cut perpendicular to the foliation and perpendicular (AW9B_1a) or parallel (AW9B_2B) to the granulite facies lineation. The sense of shear indicated within the pseudotachylyte layer is interpreted from the oblique mineral shape fabric within this layer. The lower hemisphere equal area stereoplot shows the differently oriented fracture sets A (upper side of pseudotachylyte layer) and B (lower side) and their interpreted relationship to the movement direction on the main fracture that generated the pseudotachylyte.

The studied sample has been selected from a large collection as the one best preserving pristine features of pseudotachylyte formation. It contains a single pseudotachylyte vein without any evidence for subsequent reactivation, such as overprint by ductile shearing or alteration. Crosscutting relationships establish that many of the pseudotachylytes from the Woodroffe Thrust and its hanging wall accumulated in multiple events, that generation surfaces were often reused, and that fine-grained pseudotachylytes preferentially localized subsequent aseismic ductile shear (Hawemann, Mancktelow, Pennacchioni, et al., 2019; Hawemann et al., 2018; Wex et al., 2017, 2018, 2019). In these more common examples, analyzing the microstructures that sequentially develop during an individual earthquake event and reflect the complex thermomechanical stages occurring during seismic rupture propagation and fault slip is impossible. Samples that preserve small-scale, potentially single-jerk events are relatively rare. In sample selection, we avoided pseudotachylytes from large pseudotachylyte breccia layers, which record multiple generations of frictional melts and concentrate on an individual, smaller scale vein with a simple tabular geometry. This allows a very detailed investigation of the pseudotachylyte and host rock damage over an individual thin section. The lack of post-solidification deformation of the pseudotachylyte melt and of hydrous alteration, both during pseudotachylyte development and during exhumation to the surface, has meant that microstructures on the sub-micron scale remained intact.

The sample is a weakly peraluminous, felsic granulite composed of quartz + K-feldspar + plagioclase (An 30) + garnet + biotite + kyanite + ilmenite + rutile + magnetite + hematite + apatite + zircon. This assemblage, mainly developed during the Musgravian Orogeny, shows a minor overprint in the Petermann Orogeny recorded by small amounts of scattered kyanite, rutile, and (possibly) ilmenite. The granulite foliation is defined by an alternation of quartz ribbons (a few hundreds of μm thick) with layers of predominant feldspar (plagioclase and K-feldspar). Scattered garnets of variable grain size are common (Figures 1 and 2). The single pseudotachylyte fault vein in the sample, parallel to the granulite foliation, has a thickness of ca. 1.6 mm (Figures 1 and 2). The pseudotachylyte consists of a fine-grained matrix of mainly plagioclase and K-feldspar with scattered clasts of quartz and shows an internal oblique foliation (Figures 2a, 2b, 2d and 2e). The granulite foliation carries a clear lineation (Figure 1), but there is no discernible lineation referable to the pseudotachylyte. Thin sections were cut perpendicular to the foliation and pseudotachylyte, either perpendicular (AW9B_1a) or parallel (AW9B_2b) to the granulite facies lineation (Figure 1).

Microfractures are present in both AW9B_1a and AW9B_1b, on both sides of the pseudotachylyte, at an oblique angle to the vein (Figures 1 and 2). The relationship between these fractures, the pseudotachylyte, and the granulite foliation and lineation is presented in the stereoplot of Figure 1. The sense of shear implied from the oblique foliation in the pseudotachylyte (Figures 2a, 2d and 3a) is ca. top-to-N (Figure 1) as also observed in the regional-scale Woodroffe Thrust (Figure S1 in Supporting Information S1). To allow a more direct comparison, with the exception of Figure 1, all observations from AW9B_1a are presented in mirrored form (e.g., Figure 2). The position of all figures from the thin sections is indicated in Figure 2c (AW9B_2b) and Figure 2f (AW9B_1a). High-resolution versions of all figures are available in the data repository.

## 3. Methods

Thin sections were polished initially mechanically and then for ca. 10 mins with an alkaloid colloidal suspension (Syton), before study under the scanning electron microscope (SEM). The order of the analyses was Cathode-Luminescence (CL), Secondary Electron (SE) and Back-Scattered Electron (BSE) imaging, Electron Backscatter Diffraction (EBSD) scanning, and Electron Micro-Probe Analysis (EMPA). These methods provide the

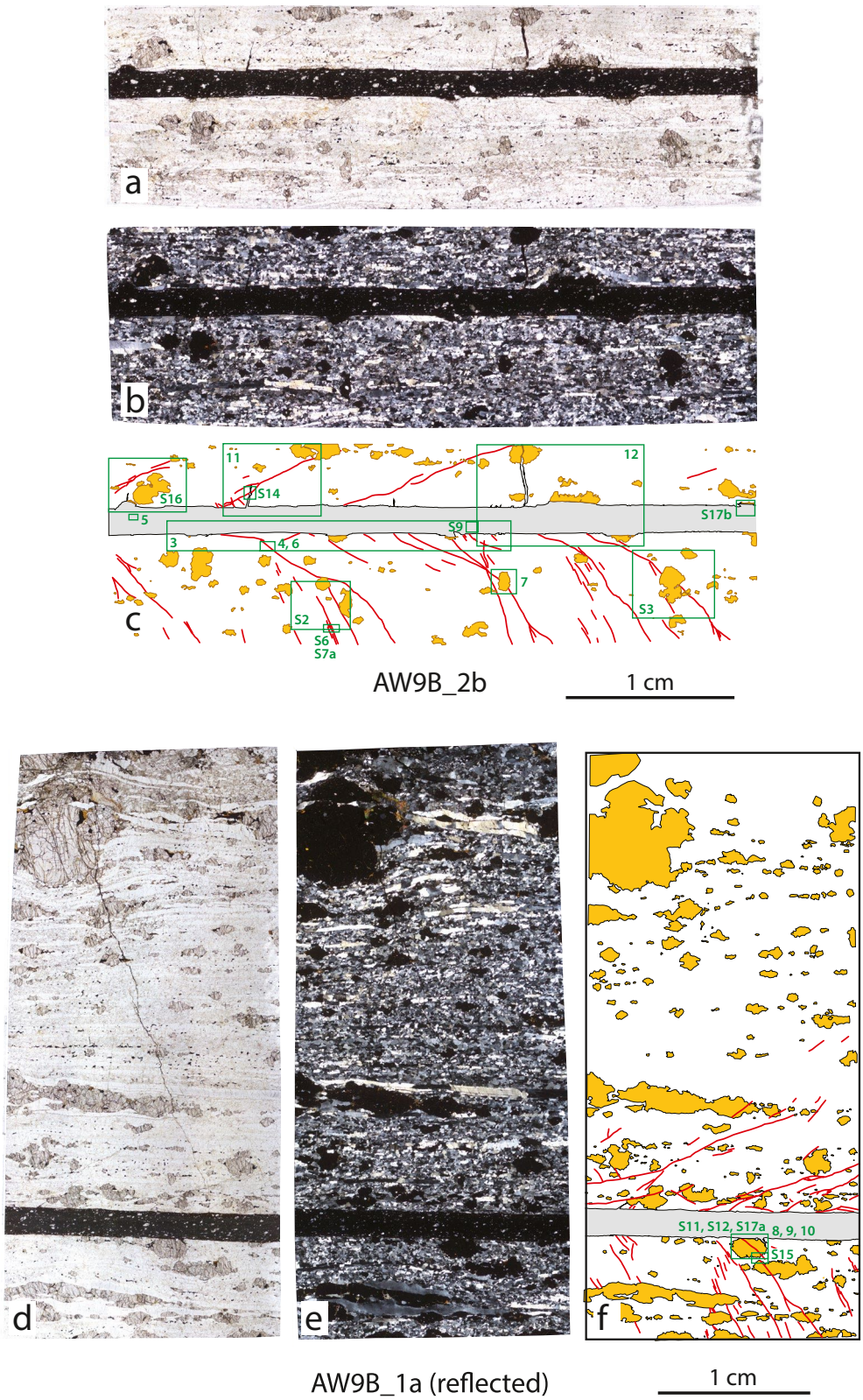


**Figure 2.** Photomicrograph mosaics of the two thin sections in plane (a), (d) and crossed polarized light (b), (e), together with the sketches from Figure 1 in (c), (f), showing locations of other figures. In (c) and (f), garnet grains are shaded in orange and fractures shown as red lines. To maintain the same relative viewpoint as in AW9B_2b, thin section AW9B_1a is reflected in Figure 2 and in all other figures in the paper.

fundamental tools for studying brittle, crystal-plastic, melt and crystallization microstructures associated with pseudotachylytes (e.g., Petley-Ragan et al., 2018, 2019, 2021; Austrheim et al., 2017; Bestmann et al., 2011, 2012; Pittarello et al., 2015; Trepmann et al., 2007; Trepmann & Stockhert, 2002). Details are given in the Supporting Information S1.

EBSD measurements were processed using the open-source program package MTEX (Bachmann et al., 2010; Hielscher & Schaeben, 2008). All EBSD crystallographic orientation maps are color coded according to the Inverse Pole Figure (IPF) legend for either garnet or quartz (hexagonal), representing the crystal orientation relative to the normal to the thin-section plane. For brevity, these maps are referred to as EBSD IPF maps. The colormap used (ipfTSLKey in MTEX) is the standard scheme of the two main commercial software packages (EDAX TSL OIM and Oxford Instruments HKL Channel 5) for direct comparison with most published work. EBSD IPF and mineral phase maps are overlain by partially transparent Image Quality (IQ) gray scale maps (Wright & Nowell, 2006) with darker tones indicating lower IQ. This can highlight spatial variation in crystal strain and more subtle substructures (Wright et al., 2011). Following the default convention in MTEX, all pole figures are upper hemisphere, equal area projections (e.g., Hentschel et al., 2019). Grains were reconstructed with the default threshold misorientation angle of 10° and subgrains with 2°. Grain boundaries in the figures are outlined in black, whereas subgrain boundaries, when shown, are outlined in red. The J-index of Bunge (1982) and the M-index of Skemer et al. (2005) were calculated to quantify the strength of the crystallographic preferred orientation (CPO) for mean grain orientations. The J-index ranges from unity (random fabric) to infinity (single crystal fabric), whereas the M-index decreases toward zero for a completely random fabric. Further details are given in the Supporting Information S1.

Grain Size Distribution (GSD; e.g., Heilbronner & Keulen, 2006), Particle Size Distribution (PSD; e.g., Blenkinsop, 1991; Buhl et al., 2013), or Clast Size Distribution (CSD; e.g., Di Toro & Pennacchioni, 2004) are fundamental data for considering mechanisms of crystal-plastic recrystallization and new grain growth (e.g., Cross et al., 2017), shear zone and fault dynamics (e.g., Aupart et al., 2018; Sammis et al., 1986), earthquake rupture (e.g., Reches & Dewers, 2005; B. R. Song et al., 2020; Wilson et al., 2005), and the origin and tectonic significance of pseudotachylyte (e.g., Behera et al., 2017; Bizzarri, 2014; Bjørnerud, 2010; Deb et al., 2015; Di Toro & Pennacchioni, 2004; Hisada, 2004; Pittarello et al., 2008; Sarkar et al., 2020). Results are typically presented as a log-log plot of the cumulative number of grains, particles, or clasts greater than a certain value versus the 2D size, given as the area or equivalent diameter (Blenkinsop, 1991; Buhl et al., 2013; Heilbronner & Keulen, 2006; B. R. Song et al., 2020; S. J. Song et al., 2017). In the current study, the grain size is represented by the diameter ($d$) of a circle equivalent to the grain area calculated with MTEX.

Cumulative plots may be continuous and well-fitted by theoretical continuous distributions, such as normal, lognormal, gamma, or Weibull distributions (e.g., Phillips & Williams, 2021). However, based on theoretical models (Turcotte, 1986) and practical observation, segments of such plots within an arbitrary "fractal range" (Blenkinsop, 1991) have been fitted by a straight line with the negative of the slope corresponding to the "fractal dimension" or $D$-value (e.g., see summary Table 1 in Buhl et al., 2013). Higher D-values indicate a larger proportion of finer material and therefore more effective grain comminution (Buhl et al., 2013).

## 4. Observations

### 4.1. Geometry and Distribution of Fractures

Two dominant sets (A and B) of discrete fractures, marked by trails of recrystallized fine quartz and feldspar, are observed over a width of ca. 1 cm to either side of the pseudotachylyte (Figures 1 and 2). The fractures of set A (upper side in Figure 1) are relatively straight, making a true angle of ca. 30° with the pseudotachylyte (stereoplot, Figure 1). The fractures of set B (lower side in Figure 1) are more curved, especially in AW9B_2b, with the angle close to the pseudotachylyte similar to a mirror image of set A. Moving away from the pseudotachylyte, and particularly in AW9B_2b, the angle of set B increases to a true angle of ca. 60° (stereoplot of Figure 1). Therefore, the maximum angle between the two fracture sets is ca. 90° with their intersection line lying in the foliation plane. A smaller number of fractures with the orientation of set B are found in the area of set A and vice versa (Figures 1 and 2).

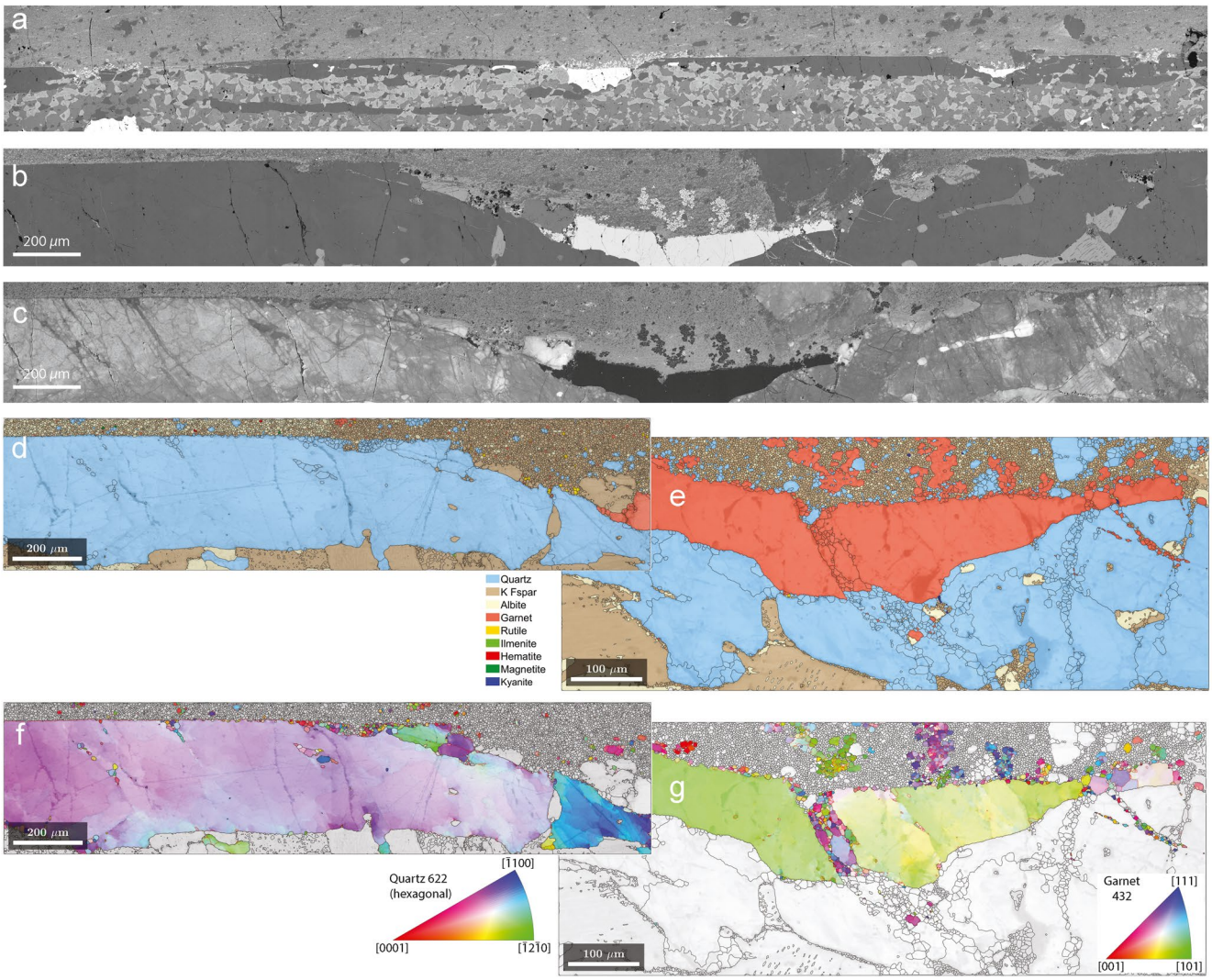


**Figure 3.** Scanning electron microscope images and Electron Backscatter Diffraction (EBSD) maps of pseudotachylyte and adjacent host rock in AW9B_2b. For location, see Figure 2c. (a) Back-Scattered Electron (BSE) mosaic overview. The main minerals, with increasingly lighter gray scale, are quartz, plagioclase, K-feldspar, and garnet. (b) BSE enlargement of the embayed garnet on the right side of (a). Note the lack of any fine structure discernible in the quartz ribbon. (c) Cathode-Luminescence image of the same area as (b). A detailed substructure marked by darker linear features, interpreted to represent healed microfractures, is now visible. (d) EBSD phase + IQ map of the left side of (c). Grains are outlined in black. (e) EBSD phase + IQ map of the central garnet in (c) with an enlargement twice that of (d). Grains are outlined in black. The garnet is not pervasively fractured adjacent to the pseudotachylyte and new grains are only developed along a distinct fracture zone parallel to set B. (f) EBSD Inverse Pole Figure (IPF) + IQ map for quartz (hexagonal) from area (d), color coded according to the Inverse Pole Figure (IPF) legend, representing the crystal orientation relative to the normal to the thin-section plane. Grains are outlined in black and subgrains in red. (g) EBSD IPF + IQ map for garnet from area (e), color coded according to the Inverse Pole Figure (IPF) legend, representing the crystal orientation relative to the normal to the thin section plane. Grains are outlined in black and subgrains in red. For (d) and (f), step size is 1.73 μm, resulting in 231,500 data points. For (e) and (g), step size is 0.87 μm, resulting in 365,806 data points.

Individual fractures transect large garnet grains (Figures 1 and 2), whereas the ductile granulite facies foliation either bends around or is overgrown by large garnets (Figures 2a, 2b, 2d and 2e). The main pseudotachylyte vein also crosscuts but locally embays into large garnet grains (Figures 1–3). Many fractures show no discernible offset (e.g., Figure S2 in Supporting Information S1). Where observed, shear offset is small (<ca. 100 μm; e.g., Figures 3e, 4a–4d, S3 in Supporting Information S1) and the sense of shear is not consistent. The shear displacement associated with the pseudotachylyte is unknown.

In quartz, the fractures are delineated by discontinuous trails of small (<30 μm) new grains. Feldspar and garnet also develop new grains along the fractures but with a much smaller grain size than quartz. Grain sizes and

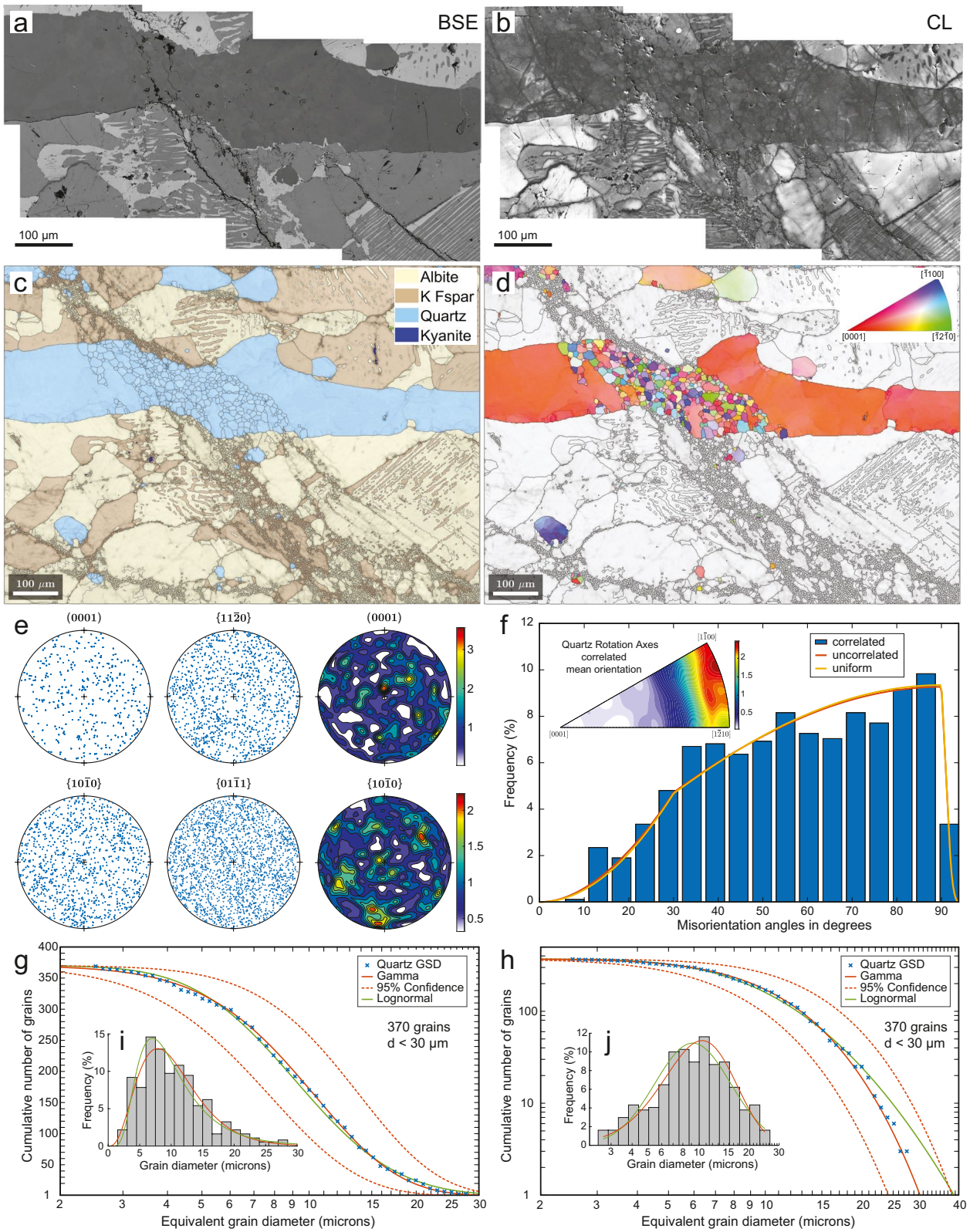
a
BSE
100 μm
b
CL
100 μm
c
Albite
K Fspar
Quartz
Kyanite
100 μm
d
[1̄100]
[0001]
[12̄10]
100 μm
e
(0001)
{11$\bar{2}$0}
(0001)
{10$\bar{1}$0}
{01$\bar{1}$1}
{10$\bar{1}$0}
f
Quartz Rotation Axes
correlated
mean orientation
correlated
uncorrelated
uniform
Frequency (%)
Misorientation angles in degrees
g
Quartz GSD
Gamma
95% Confidence
Lognormal
370 grains
d < 30 μm
Cumulative number of grains
Equivalent grain diameter (microns)
i
Frequency (%)
Grain diameter (microns)
h
Quartz GSD
Gamma
95% Confidence
Lognormal
370 grains
d < 30 μm
Cumulative number of grains
Equivalent grain diameter (microns)
j
Frequency (%)
Grain diameter (microns)

**Figure 4.**

grain size distributions for quartz, feldspar, and garnet are considered quantitatively below for direct comparison with analogous data from previous studies of seismic faults and pseudotachylytes (e.g., Di Toro & Pennacchioni, 2005; B. R. Song et al., 2020).

SEM-CL images record much more extensive fracturing in quartz and feldspar than is discernible in BSE images or under the optical microscope (Bestmann et al., 2012, 2016). In CL images, healed microfractures are visible as linear features darker than the pristine quartz and feldspar (Figure 3c, Figures S2b, S2d–S2f in Supporting Information S1; Bestmann et al., 2016). The CL patterns and microstructures mapped by EBSD in quartz ribbons are not discernibly modified approaching the contact to the pseudotachylyte, but are sharply transected (Figures 3c and 3f). Healed microfractures in quartz and feldspar are parallel to, or extend into, trains of recrystallized grains (Figures 3c, 3f, 4b, 4c, 4d, 5b and 5d) but do not overprint these recrystallized grains (Figure 4b). The microfractures also affect garnet and are visible in CL within quartz inclusions hosted by garnet (Figures S2b, S2e and S2f in Supporting Information S1).

The few biotite grains in the host rock are strongly kinked throughout the thin section. Such kinking of mica has been already reported in other studies of pseudotachylyte (e.g., Anderson et al., 2021; Bargossi et al., 1982; Bestmann et al., 2011; Di Toro & Pennacchioni, 2005; Passchier, 1982).

### 4.2. Fractures in Quartz Within the Host Rock

#### 4.2.1. Crystallographic Orientation Data

Recrystallized quartz grains within fractures transecting the quartz ribbons have a random CPO (Figure 4e) and random misorientation angles both between correlated, neighboring grains (J-index 1.21, M-index 0.0051) and between uncorrelated grains (J-index 1.18, M-index 0.0047; Figure 4f). The rotation axis between neighboring grains is also incoherent and random (inset Figure 4f, compare to Figure S4a in Supporting Information S1). The grain orientation spread (GOS) in the small grains ($d < 30$ μm) is distinctly lower than in the larger host grains (Figures S5a and S6e in Supporting Information S1).

Evidence for subgrain rotation is lacking. Some subgrains, with a size similar to recrystallized grains along the fracture, occur within the host grain (Figures 4d, S6c and S7 in Supporting Information S1), but generally not adjacent to the new grains (Figures 4d, S6c in Supporting Information S1). As noted above, the rotation axis for neighboring grains is not related to a coherent crystallographic direction (Figure 4f).

#### 4.2.2. Grain Size Distribution

The GSD of recrystallized quartz grains along fractures shows a continuous change in slope (Figures 4g and 4h) without any clear straight segment on the log-log plot (Figure 4h). This is the case for all 5 analyzed locations (Figure S8 in Supporting Information S1). The data are well-fitted by either a continuous gamma or Weibull distribution. This is true for individual areas (Figures 4g–4j, S6g, S6h and S8a in Supporting Information S1) but is better defined for the cumulative data set (Figure S8b in Supporting Information S1). For grain sizes less than ca. 20 μm, there is no significant difference in the log-log GSD plot between gamma, Weibull, and lognormal distributions (Figure S8b in Supporting Information S1) and the great majority of grains (>90%) are almost equally well described by a lognormal distribution. However, the GSD for the (few) largest grains ($d >$ ca. 20 μm) is better fitted by a Weibull distribution (Figure S8b in Supporting Information S1), which implies that there are fewer larger grains than would be predicted by gamma or lognormal distributions. This is not just due to the

**Figure 4.** Scanning electron microscope images, Electron Backscatter Diffraction (EBSD) data, and Grain Size Distribution (GSD) plots for quartz from a fracture zone of set B that crosscuts a quartz ribbon and adjacent feldspar. Thin section AW9B_2b; for location, see Figure 2c. (a) Back-Scattered Electron image. (b) Cathode-Luminescence image. Note the much greater microstructural detail visible in both quartz and feldspar. (c) EBSD phase + IQ map. (d) EBSD IPF + IQ map for quartz (hexagonal). The step size in (c) and (d) is 1.3 μm, resulting in 395,580 data points. (e) Scatter and contoured pole figures for quartz new grains ($d < 30$ μm; $n = 370$) in the quartz ribbon, demonstrating an effectively random distribution. (f) Misorientation angle plot of correlated, neighboring grains (895 pairs), uncorrelated grains (Misorientation Distribution Function for mean orientation per grain), and a uniform distribution. The rotation axes between grains for the correlated case are plotted in the inset, which approximate a random distribution. (g) Linear-log plot of quartz cumulative GSD for new grains developed in the quartz ribbon ($d < 30$ μm). (h) Log-log plot of quartz cumulative GSD for new grains developed in the quartz ribbon ($d < 30$ μm). (i) Histogram of relative frequency versus grain size (equivalent grain diameter $d$) with the best-fit lognormal and gamma continuous distributions plotted (j) Histogram of relative frequency versus log grain size (equivalent grain diameter $d$) with the best-fit lognormal and gamma continuous distributions plotted.

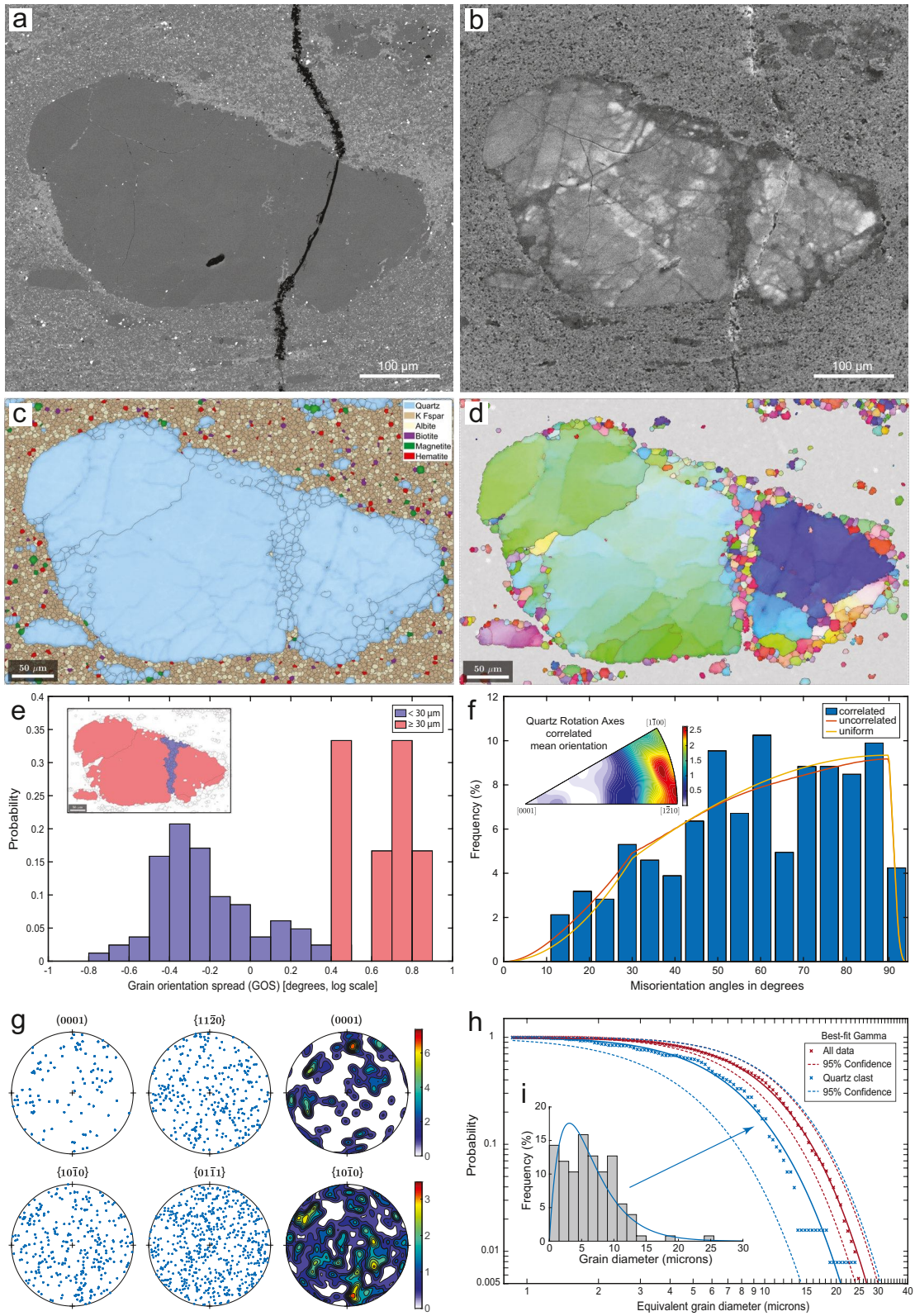
a
100 μm
b
100 μm
c
Quartz
K Fspar
Albite
Biotite
Magnetite
Hematite
50 μm
d
50 μm
e
< 30 μm
≥ 30 μm
Probability
Grain orientation spread (GOS) [degrees, log scale]
f
Quartz Rotation Axes
correlated
mean orientation
correlated
uncorrelated
uniform
Frequency (%)
Misorientation angles in degrees
g
(0001)
{11$\bar{2}$0}
(0001)
{10$\bar{1}$0}
{01$\bar{1}$1}
{10$\bar{1}$0}
h
Best-fit Gamma
All data
95% Confidence
Quartz clast
95% Confidence
Probability
i
Frequency (%)
Grain diameter (microns)
Equivalent grain diameter (microns)

**Figure 5.**

data limitations involved in sampling larger grain sizes. As is clear qualitatively from Figures 4d, S6c and S7 in Supporting Information S1 as well as quantitatively from the GSD plots, there are few large new grains and there is a true limit to the maximum grainsize, so that the new grains are all captured in a plot with $d < 30$ μm.

The RMS grain diameter for the 370 new quartz grains of Figure 4 is 11.6 ± 5.2 μm (±1 standard deviation). The value for the 1491 grains from all 5 analyzed locations (Figure S8b in Supporting Information S1) is 10.50 ± 4.93 μm. The mean from the best-fit gamma distribution for Figures 4g–4j is 10.4 ± 5.1 μm and 9.23 ± 4.98 μm for all areas. The mean from the best-fit Weibull distribution for all areas (Figure S8b in Supporting Information S1) is 9.26 ± 4.86 μm and is well within error of the best-fit gamma distribution (Figure S8b in Supporting Information S1). The range of RMS grain diameters for individual data sets is from 11.7 to 8.3 μm and for the mean of the gamma distribution from 10.6 to 7.3 μm.

### 4.3. Quartz Clasts Within the Pseudotachylyte

#### 4.3.1. Geometry

Clasts within the pseudotachylyte are exclusively quartz (e.g., Figures 3a, 3d, 3e and 5) and preserve the same microstructure as in the host quartz ribbons, including sets of healed microfractures parallel to trails of recrystallized quartz (Figures 5b–5d). Quartz clasts have generally segmented along such already recrystallized healed fractures (Figures 5a–5d) but locally fractures developed in pristine quartz without associated recrystallization (Figures S9c and S9d in Supporting Information S1).

#### 4.3.2. Crystallographic Orientation Data

Similar to the host rock, the misorientation plot for uncorrelated grains from the localized zone of recrystallization in the quartz clast of Figure 5f is close to random, although the statistics is limited by the small number of grains (105). The CPO of the new grains is also random (Figure 5g). Using the mean orientation of grains, the calculated J-index is 1.70 and the M-index is 0.019. The rotation axis for correlated grains is also random (inset, Figure 5f). The GOS in the small grains ($d < 30$ μm) within the localized zone is distinctly lower than that in the larger host grains (Figure 5e).

#### 4.3.3. Grain Size Distribution

As within the host-rock, the GSD for the recrystallized quartz along healed fractures in clasts is well-fitted by a continuous gamma distribution (Figures 5h and 5i). New quartz grains within the analyzed clast (Figure 5) have an RMS grain diameter of 7.5 ± 4.1 μm and a mean from the best-fit gamma distribution of 6.4 ± 3.9 μm, which is below the range obtained for the 5 areas from the host rock. However, because of the small number of grains, the uncertainty is significant (Figure 5h) and the results from the quartz clast are indistinguishable from that of the summed host-rock data set at the 95% confidence level.

**Figure 5.** Scanning electron microscope images, Electron Backscatter Diffraction (EBSD) data, and Grain Size Distribution (GSD) plots for an isolated larger quartz clast within the main pseudotachylyte vein. Thin section AW9B_2b; for location, see Figure 2c. (a) Back-Scattered Electron image (b) Cathode-Luminescence image. Note the dark lines interpreted as healed microfractures, similar to those in the country rock, and the narrow zone of new quartz grains parallel to these dark lines, which are also interpreted to mark an earlier fracture. (c) EBSD phase + IQ map. Note that the pseudotachylyte is dominated by K-feldspar and plagioclase ("albite") with small amounts of biotite, magnetite, and hematite. (d) EBSD IPF + IQ map for quartz (hexagonal). IPF color code map is for quartz (hexagonal), as given in Figure 4d. The step size in (c) and (d) is 1.73 μm, resulting in 51,675 data points. (e) GOS for larger (pink; $d \geq 30$ μm; $n = 6$) and smaller (mauve; $d < 30$ μm; $n = 105$) grains within the clast. (f) Misorientation angles for correlated (283 neighbor pairs) and uncorrelated smaller new grains with $d < 30$ μm, indicating an effectively random texture. The axes of rotation between correlated grains are also effectively random (inset). (g) Scatter and contoured pole figures for the 105 smaller ($d < 30$ μm) new quartz grain orientations with an effectively random distribution. (h) Comparison between the GSD for the smaller new grains ($d < 30$ μm, mauve) in the clast and the GSD for all data on new quartz grains in the country rock (Figure S8b in Supporting Information S1). The GSD of new quartz within the clast is similar to that for all other measurements in the country rock, within the 95% confidence limits. (i) Histogram of relative frequency versus grain size for the smaller new grains ($d < 30$ μm) in the clast with the best-fit gamma continuous distribution plotted.

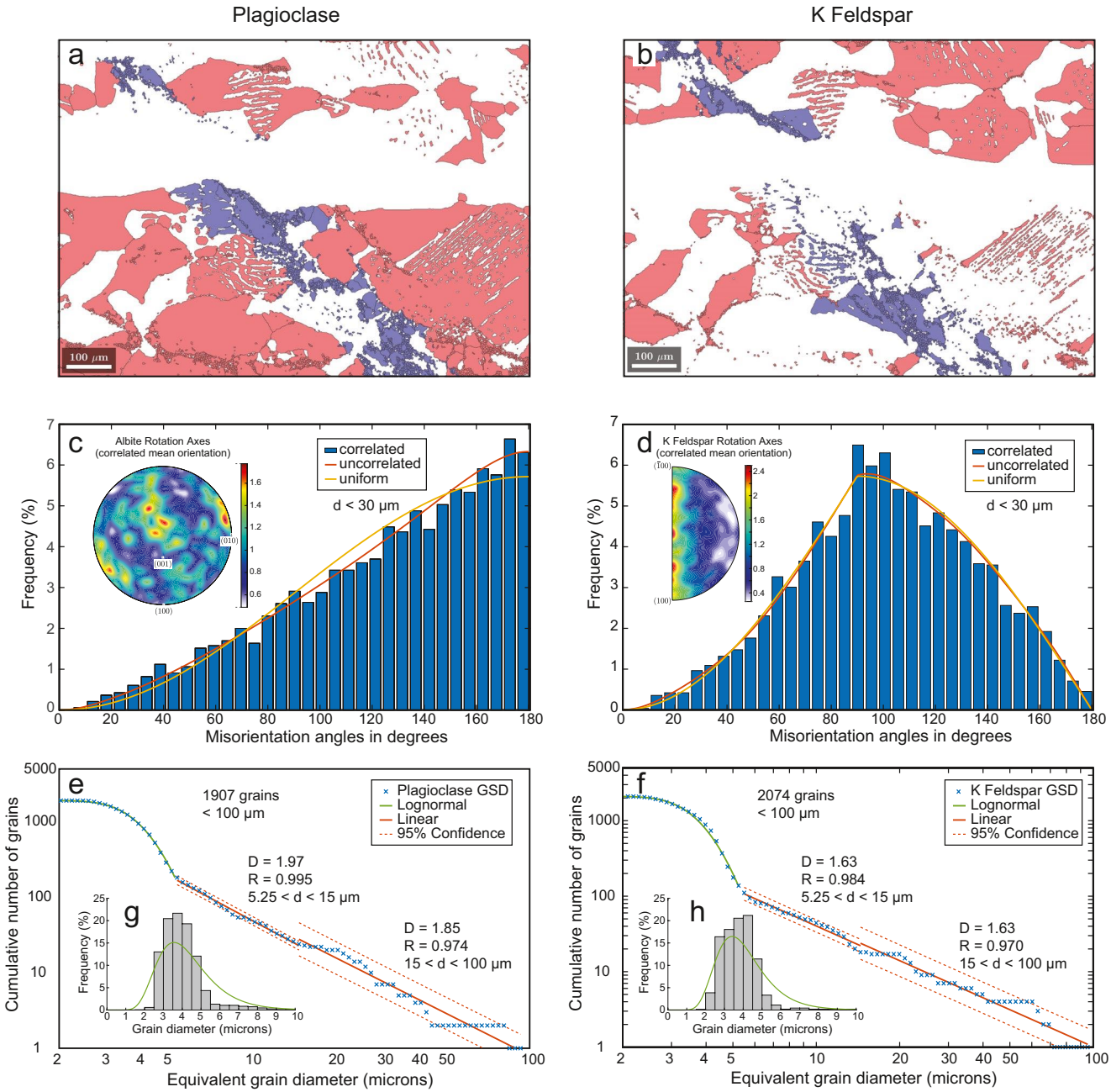


**Figure 6.** Misorientation and Grain Size Distribution (GSD) plots for feldspar from the fracture zone of Figure 4. Grains shown in mauve with $d < 100$ μm from a region along the fracture zone for (a) plagioclase (indexed in Electron Backscatter Diffraction as albite) and (b) K-feldspar are those considered in the subsequent plots. (c) Misorientation angle plot of plagioclase grains with $d < 30$ μm for correlated, neighboring grains (3,374 pairs), uncorrelated grains (Misorientation Distribution Function [MDF] for mean orientation per grain) and for a uniform distribution. The rotation axes between correlated grains are plotted in the inset and are effectively random. (d) Misorientation angle plot of K-feldspar grains with $d < 30$ μm for correlated neighboring grains (3,290 pairs), uncorrelated grains (MDF for mean orientation per grain), and for a uniform distribution. The rotation axes between correlated grains are plotted in the inset and are effectively random. (e) GSD log-log plot for plagioclase grains with $d < 100$ μm. (f) GSD log-log plot for K-feldspar grains with $d < 100$ μm. (g) Histogram of relative frequency versus grain size for the plagioclase grains of (e) with the best-fit lognormal continuous distribution plotted. (h) Histogram of relative frequency versus grain size for the K-feldspar grains of (f) with the best-fit lognormal continuous distribution plotted.

#### 4.3.4. Clast Size Distribution

The CSD of quartz clasts within the pseudotachylyte, rather than individual grains, was measured by merging neighboring quartz grains into amalgamated clasts (Figure S9 in Supporting Information S1). Arbitrarily, grains

with a shared boundary shorter than 4 μm and with less than 25% of their perimeter in common were excluded from the merge. This avoids unifying "clasts" that are impinging on only a short common boundary. For good statistics, the results from 7 different areas were combined for a total of 3,431 clasts (Figure S9f in Supporting Information S1). Unlike the GSD cumulative plot for the recrystallized grains (Figures 4h and 5h, S8 in Supporting Information S1), the CSD shows a linear distribution on the log-log plot for $2.5 < d < 50$ μm, both for individual areas (Figure S9e in Supporting Information S1) and especially for the larger combined data set (Figure S9f in Supporting Information S1). For the combined data, the D-value is 1.7 with a correlation coefficient of 0.9992 (Figure S9f in Supporting Information S1). The RMS diameter for all the clasts is 13.1 ± 12.5 μm, with the large standard deviation reflecting a broad spread in clast size (Figure S9e and S9f in Supporting Information S1). For a lognormal distribution fit to the full data set (Figure S9f in Supporting Information S1), the mean clast diameter is 3.39 ± 3.56 μm, reflecting the large number of small quartz clasts in the pseudotachylyte. It is probable that the large number of clasts with $d < 2.5$ μm, which are below the linear "fractal range" (Blenkinsop, 1991) on Figure S9f in Supporting Information S1, are not actually clasts but new grains that have crystallized from the pseudotachylyte melt. However, there was no criterion to make a clear distinction.

### 4.4. Fractures in Feldspar

#### 4.4.1. Geometry

The fracture pattern in feldspar mimics that in quartz as is also clear in the CL images (e.g., Figure 4b). However, because the recrystallized grain size is distinctly smaller than in quartz, the trains of new grains marking fractures tend to be narrower, forming a braided network of anastomosing fine fractures extending from broader zones of quartz recrystallization (Figures 4c and 4d).

#### 4.4.2. Crystallographic Orientation Data

The new smaller ($d < 30$ μm) feldspar grains are randomly oriented. For the example of Figure 6, the recrystallized plagioclase grains have a J-index of 2.27 and an M-Index of 0.033 for correlated grains and a J-index of 2.16 and an M-index of 0.035 for uncorrelated grains. K-feldspar has a J-index of 1.73 for correlated grains and 1.69 for uncorrelated grains, whereas the M-index for both correlated and uncorrelated grains is 0.009. Such low values of the M-index indicate that, for uncorrelated grains, the misorientation is effectively random. The plots of Figures 6c and 6d show that, for correlated grains, the misorientation angle and corresponding rotation axis between grains are also random. The GOS in the small grains ($d < 5.25$ μm) is distinctly lower than that in the larger grains (Figures S5b and S5c in Supporting Information S1), supporting the textural observation that these are new grains developed along fractures.

#### 4.4.3. Grain Size Distribution

The GSD and grain size histograms for the two feldspars from the same fracture zone are very similar (Figures 6e–6h). The great majority of grains with $d < 5.25$ μm shows a GSD with a continuous change in slope on the log-log plot that is well-fitted by a lognormal distribution (similar to the small, recrystallized quartz grains along the same fracture zone). However, the less numerous larger grains (ca. 100–150 from a total of ca. 2000; Figures 6e and 6f) show a good linear fit, especially in the range $5.25 < d < 15$ μm. In Figure 6, the RMS grain diameter for $d < 5.25$ μm is 3.73 ± 0.74 μm (plagioclase) and 3.75 ± 0.73 μm (K-feldspar). The D-value for $5.25 < d < 15$ μm is 1.97 (plagioclase) and 1.63 (K-feldspar). The grain size of the numerically dominant smaller grains is therefore identical for the two feldspars, but the D-values for the larger grains are slightly different.

For the combined data set of plagioclase and K-feldspar (Figure S10 in Supporting Information S1), the single regression line for $5.25 < d < 100$ μm (with correlation coefficient 0.9972) shows a slope $D = 1.67$, identical to the D-value obtained for quartz clasts within the pseudotachylyte (Section 4.3.4; Figure S9 in Supporting Information S1). The RMS grain size for all feldspar with $d < 5.25$ is 3.78 ± 0.71 μm and the mean from the best-fit lognormal distribution is 3.72 ± 0.74 μm. These values are identical to those for individual plagioclase and K-feldspar, reinforcing the observation that there is no difference in the grain size statistics between the two feldspars.

### 4.5. Fractures in Garnet

#### 4.5.1. Geometry

Fractures defined by trains of recrystallized grains in quartz and feldspar also crosscut granulite facies garnet grains (Figures 1, 2, 7, S3 and S11 in Supporting Information S1). Additional secondary fractures within garnets do not always extend into the surrounding quartz or feldspar (e.g., Figures 7, 8). In Figure 7a, the main fracture (brown arrow) in the garnet sinistrally offsets the garnet boundaries and is continuous into the surrounding rock, corresponding to a well-defined fracture of the set B (Figure 1). The subsidiary fracture (black arrow; Figure 7a), which has the orientation of fracture set A (Figure 1), does not offset the quartz inclusion into which it runs (Figure 7b) or the garnet grain boundary, and has no discernible continuation outside the garnet. Despite the lack of offset, the quartz inclusion shows a whole set of internal healed fractures (dark lines in CL, Figure 7b) that are parallel to the much more widely spaced, discrete fractures in the surrounding garnet grain.

Subgrains and new grains are irregularly developed along the main fractures in garnet (Figures 7, 8, S3e, S11b and S12b in Supporting Information S1). The fractures in garnet form a planar array, and the garnet and quartz inclusions removed from these fractures remain little affected (e.g., quartz inclusion "1" in Figure 8). Garnet immediately adjacent to the main pseudotachylyte vein is locally transected by discrete fractures (Figures 3e and 3g) but is not shattered. Pervasive fragmentation of garnet in close proximity to the pseudotachylyte vein is not observed (Figures 3, 7, 8, S11b in Supporting Information S1). However, localized garnet pulverization related to fracture intersections does occur in one location and is described in detail below (Section 4.5.4).

#### 4.5.2. Crystallographic Orientation Data

The new grains along the main fracture in Figure 7 all have a grain size $d < 30$ μm and an overall random orientation (Figures 7h–7l). For uncorrelated grains in Figure 7i, the curve for the Misorientation Distribution Function (MDF) calculated for mean orientation (i.e., one point per grain) is indistinguishable from the uniform distribution, with J-index of 1.11 and M-index of 0.011. However, in contrast to quartz and feldspar, the correlated new garnet grains do show a weak preference for smaller misorientation angles and the rotation axes are preferentially around the [111] and [101] axes (Figure 7i), although the corresponding changes in the J-index (1.16) and M-index (0.073) are small. The subgrain microstructure outlined by the red lines in Figure 7h also suggests a component of recrystallization by progressive subgrain rotation.

#### 4.5.3. Grain Size Distribution

For the range from $2 < d < 16$ μm, there is a good linear fit ($R = 0.997$) on the log-log plot of the GSD with a D-value of 2.34 (Figure 7k). However, the majority of grains with $d < 2$ μm shows a more continuous distribution, similar to that observed in feldspar, which can be fitted with a lognormal distribution. The RMS grain diameter for the 1066 new small garnet grains of Figure 7k is $3.04 \pm 1.98$ μm, and the mean to the best-fit lognormal distribution (Figures 7k and 7l) is $2.24 \pm 1.34$ μm. If all 3,762 grains from 10 different analyzed EBSD areas are used, the results are $D = 2.59$ with $R = 0.9981$ for $2 < d < 25$ μm (Figure S13a in Supporting Information S1); if the range is split, then $D = 2.28$ with $R = 0.9998$ for $2 < d < 8.5$ μm and $D = 2.77$ with $R = 0.9946$ for $8.5 < d < 25$ μm (Figure S13b in Supporting Information S1). Alternatively, an improved fit for the whole data range $2 < d < 30$ μm is given by a lognormal or Weibull distribution (Phillips & Williams, 2021). However, as seen from Figure S13 in Supporting Information S1, the divergence from tightly defined linearity that occurs for $d > 8.5$ μm only corresponds to ca. 40 larger grains out of a total of 3,762. The combined data echoes the observation that there is no linear fit for finer grain sizes below ca. 2 μm, and these smaller grains in fact represent the great majority.

#### 4.5.4. Localized Garnet Pulverization and Injection

Pulverization occurred in local zones of dilatation at fracture intersections as in the garnet shown in Figure 8. The quartz inclusion "2" in this garnet (Figure 8b) was shattered between two intersecting fractures (Figures S11 and S12 in Supporting Information S1) and shows a pull-apart space filled with ultrafine garnet grains (Figures 9c–9f)

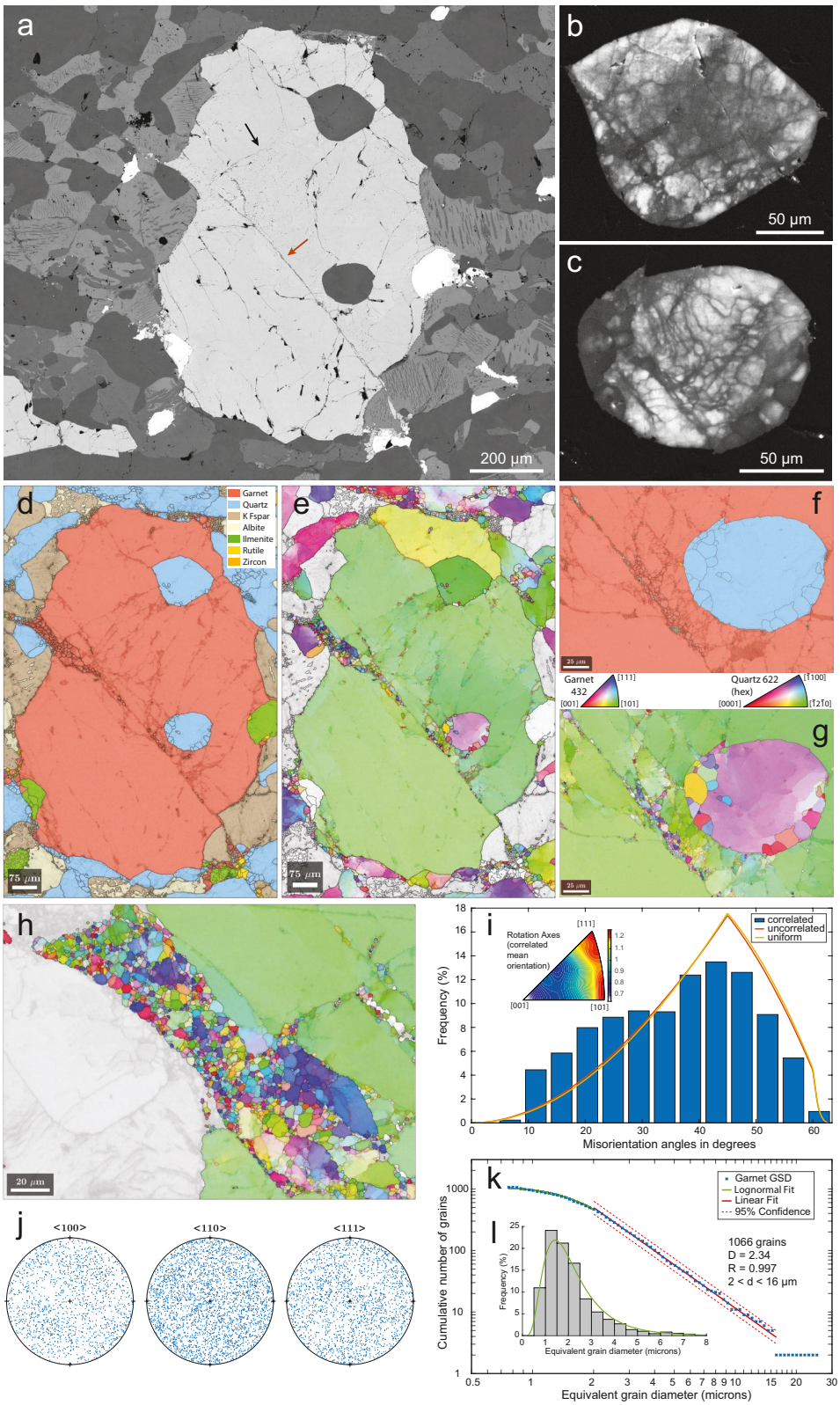
a
200 μm
b
50 μm
c
50 μm
d
Garnet
Quartz
K Fspar
Albite
Ilmenite
Rutile
Zircon
75 μm
e
75 μm
f
25 μm
Garnet
432
[001]
[111]
[101]
Quartz 622
(hex)
[0001]
[1100]
[1210]
g
25 μm
h
20 μm
i
Rotation Axes
(correlated
mean
orientation)
[111]
[001]
[101]
correlated
uncorrelated
uniform
Frequency (%)
Misorientation angles in degrees
j
<100>
<110>
<111>
k
Garnet GSD
Lognormal Fit
Linear Fit
95% Confidence
Cumulative number of grains
Equivalent grain diameter (microns)
l
1066 grains
D = 2.34
R = 0.997
2 < d < 16 μm
Frequency (%)
Equivalent grain diameter (microns)

**Figure 7.**

identical in composition to the enclosing garnet (Table S1 in Supporting Information S1). Only garnet and quartz were involved and no hydrous minerals developed (Figures 9c–9f). Figure 10 presents the EBSD results from the garnet-filled pull-apart. The crystallographic orientation of the fine garnet grains is random (Figure 10d). For the range $0.45 < d < 4$ μm, the D-value is 2.9 ($R = 0.995$; Figure 10e), which is somewhat higher than the value obtained for binned results for the small size fraction from other garnet fractures ($D = 2.59$; Figure S13a in Supporting Information S1). The lower limit to the linear segment on the log-log plot is also at a smaller grain size. Overall, the average grain size is much smaller in this zone of pulverization with an RMS grain diameter of $0.45 \pm 0.28$ μm and a mean to the best-fit lognormal distribution of $0.28 \pm 0.08$ μm (Figure 10f).

### 4.6. New Mineral Growth Along Fractures and Grain Boundaries

Fractures commonly show the growth of new quartz, plagioclase, K-feldspar, kyanite and less commonly garnet, ilmenite, and rutile (Figure 11). Garnet along fractures has a dendritic or cauliflower shape, similar to garnet within the pseudotachylyte (Figure 11b). Cauliflower garnets from both sites are enriched in Ca relative to the granulite facies garnet (Table S1 in Supporting Information S1), consistent with higher pressure conditions during the Petermann Orogeny (ca. 650°C, 1.2 GPa; Camacho et al., 2009; Hawemann et al., 2018). Fractures within garnet locally contain new feldspar, magnetite, and rutile (Figures 7f and 8b). The growth of these minerals, especially in a monomineralic host, such as garnet (Figure 7f) or K-feldspar (Figure 11c), implies the redistribution of chemical components as also imaged in EMPA chemical maps (Figures 11e and 11f, S14 in Supporting Information S1).

The fractures are marked by increased grain boundary porosity in the recrystallized aggregates (Figures 11c and 11d, S15 and S16 in Supporting Information S1). This porosity is locally bridged by kyanite needles, which are not extended and fractured (Figures 11c and 11d, S16d in Supporting Information S1). The dilatant grain boundary space is locally filled with fibrous material linking matching sides of the boundaries and demonstrating dominantly tensile opening (Figures 11d, S16d in Supporting Information S1). This intergranular material is darker in BSE images than plagioclase (Figures 11d), and spot Energy Dispersive X-Ray Analysis (EDX) shows a strong enrichment in $SiO_2$.

In Figure 11a, the pseudotachylyte injection vein crosscuts the main fracture and several minor, parallel smaller-scale fractures without diverging or following these earlier cracks. The enhanced porosity and chemical change, typically involving enrichment in $SiO_2$, does not crosscut the pseudotachylyte injection vein, as is confirmed by the EMPA chemical maps of Figure S14 in Supporting Information S1. This is also reflected in the lack of new mineral growth (kyanite fibers, quartz, plagioclase, K-feldspar, garnet, ilmenite, or rutile), impinging into the pseudotachylyte vein. Therefore, vein injection post-dated fracture, chemical alteration, and new mineral growth.

Opened boundaries are observed not only between new grains along fractures but also between original relict grains. These opened and reacted grain boundaries are subparallel to discrete fractures of sets A and B and are not uncommonly the direct continuation of intracrystalline fractures (Figures 11, S15 and S16 in Supporting Information S1). The opened boundaries do not show discernible shear offset (Figures S15 and S16 in Supporting Information S1). They are also associated with the introduction and removal of chemical components and growth of new minerals, most typically plagioclase, quartz, and fibrous kyanite (e.g., Figure S15c in Supporting

**Figure 7.** Scanning electron microscope images, Electron Backscatter Diffraction (EBSD) data, and Grain Size Distribution (GSD) plot from a fractured garnet in the pseudotachylyte host rock. Thin section AW9B_2b; for location, see Figure 2c. (a) Back-Scattered Electron overview. Note the two large quartz inclusions and the main crosscutting fracture (brown arrow), causing sinistral offset of the garnet boundary. A secondary fracture that does not offset the boundary of the garnet or of the quartz inclusions is indicated by a black arrow. (b) Cathode-Luminescence (CL) image of the quartz inclusion in the upper right area. Note the two preferential orientations of black lines (healed microfractures) parallel to the main and secondary fractures. (c) CL image of the quartz inclusion in the center right area. Again note the two preferential orientations of black lines (healed microfractures) parallel to the main and secondary fractures. (d) EBSD phase + IQ map. (e) EBSD IPF + IQ map for garnet and quartz (hexagonal). The step size in (d) and (e) is 1.73 μm, resulting in 284,416 data points. (f) Enlargement of the phase map to show the presence of K-feldspar, plagioclase, magnetite, and rutile along the main fracture. (g) EBSD IPF + IQ map for garnet and quartz (hexagonal) from the same enlarged area. The step size in (f) and (g) is 0.43 μm, resulting in 224,393 data points. (h) EBSD IPF + IQ map for garnet from the enlarged area toward the top left of the main fracture, where the garnet is strongly recrystallized. The step size is 0.43 μm, resulting in 144,974 data points. (i) Misorientation angle plot for grains with $d < 30$ μm from the region of (h); inset shows the rotation axes for correlated (neighboring) grains (2632 pairs). (j) Pole figures for 500 randomly selected garnet grains with $d < 30$ μm from (h). (k) Log-log plot of the GSD for garnet grains with $d < 30$ μm from the region of (h). (l) Histogram of relative frequency of garnet grain sizes (linear scale) with best-fit lognormal distribution indicated.

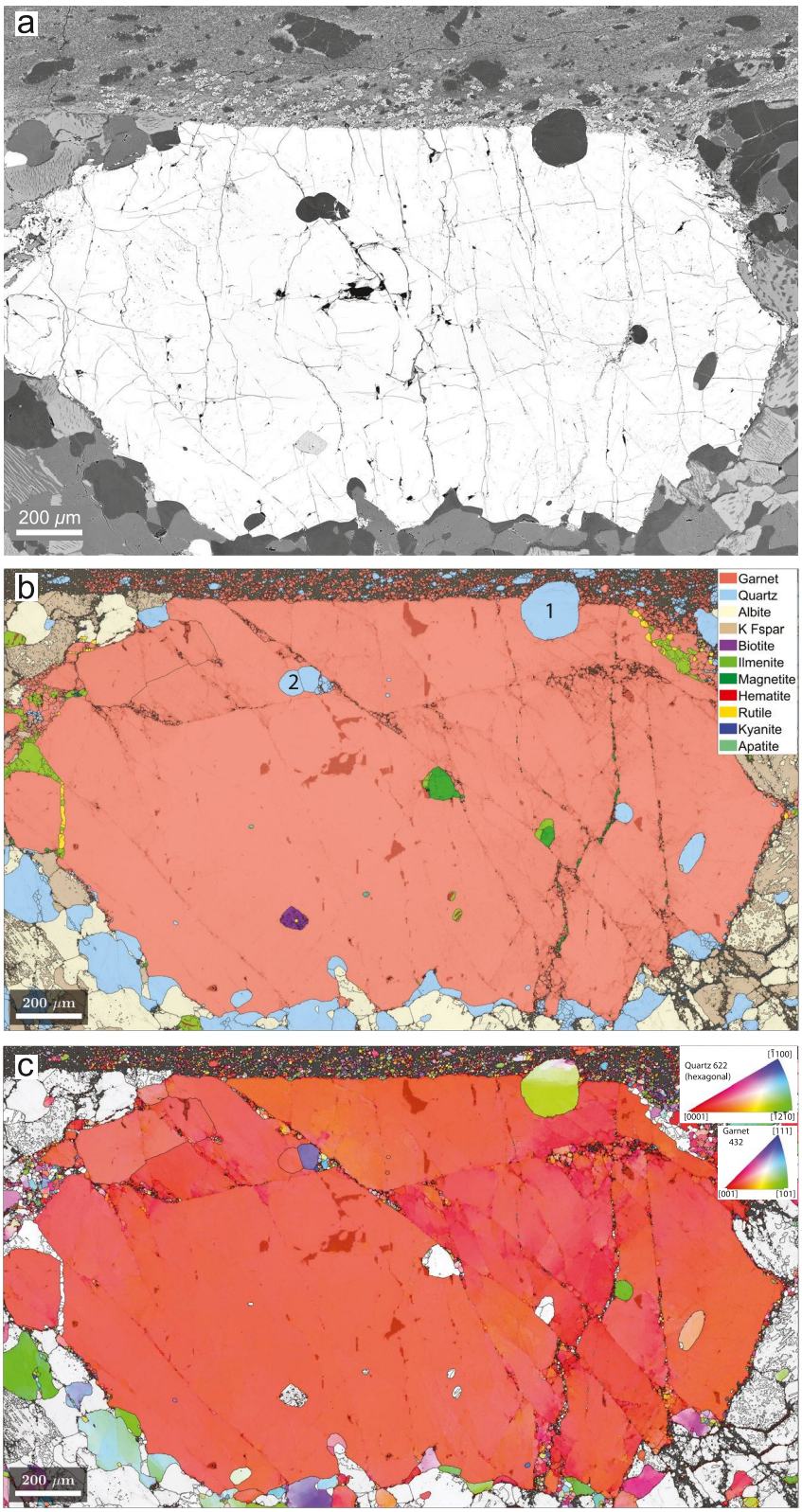
a
200 μm
b
1
2
Garnet
Quartz
Albite
K Fspar
Biotite
Ilmenite
Magnetite
Hematite
Rutile
Kyanite
Apatite
200 μm
c
Quartz 622
(hexagonal)
[0001]
[$\bar{1}$2$\bar{1}$0]
[$\bar{1}$100]
Garnet
432
[001]
[101]
[111]
200 μm

**Figure 8.**

Information S1). Similar to the discrete fractures, the opened and reacted grain boundaries appear to be crosscut by pseudotachylyte injection veins (Figures 11 and 12).

### 4.7. Melting and Pseudotachylyte Formation

The pseudotachylyte is most commonly delimited by a sharp, straight boundary with quartz ribbons or, less commonly, feldspar of the host rock, but invariably shows embayments into large host rock garnets (Figures 3 and 12). The contrast in behavior of garnet and quartz adjacent to the pseudotachylyte vein is clearly demonstrated in Figures 8, 9a and 9b, where an original quartz inclusion within garnet now protrudes into the pseudotachylyte. This quartz grain has remained almost pristine, with only minor healed microfractures visible by CL (Figure 9b). The portion of the quartz grain protruding into the pseudotachylyte is slightly dextrally sheared with the deformation accommodated by minor intracrystalline plasticity, but without development of subgrains or recrystallization (Figure 8c).

Planar fractures in host rock garnet are associated with strong and localized grain size reduction (Figures 3g, 7e, and 8c). However, where these fractures intersect the pseudotachylyte there is little indication for localized embayment that would indicate preferential melting of the finer grained garnet along the fracture (Figures 3g and 8).

Small injection veins of pseudotachylyte are mostly developed on the upper side of the pseudotachylyte fault vein (Figures 1, 2 and 12). The injection veins are predominantly perpendicular to the main pseudotachylyte and crosscut fractures of sets A or B (Figures 1, 2 and 11). Rare injection veins on the lower side are very short and mainly localized on the boundaries of host rock large garnet grains. The relatively large injection vein shown in Figure 12 has injected a large relict garnet at a distance of ca. 3 mm from the main pseudotachylyte. As can be seen in Figures 12b and 12c, the vein bifurcates within the garnet, guided by minor conjugate fractures that are only present within the garnet. The acute angle between these conjugate fractures is small (ca. 40° in the plane of the thin section). The bisector of this acute angle is approximately parallel to the injection vein and therefore perpendicular to the main vein.

### 4.8. Flow and Solidification of the Pseudotachylyte

The pseudotachylyte solidified and crystallized a fine-grained matrix composed of plagioclase and K-feldspar with minor amounts of garnet, kyanite, magnetite, hematite, ilmenite, rutile, and biotite. The grain size of the feldspar matrix is ca. 2 μm, although it should be noted that the employed EBSD resolution does not allow robust grain size characterization for $d < 2$ μm. The pseudotachylyte matrix is heterogeneous and modal variation in plagioclase and K-feldspar defines an oblique, planar layering consistent with dextral shearing for the chosen orientation of figures. K-feldspar is typically concentrated in the strain shadows of quartz clasts in this sheared flow fabric (Figures 3a, 8 and 12a, S17 in Supporting Information S1). More elongate quartz clasts are moderately aligned and in part define the foliation, but many more equant clasts were not elongated by the flow (Figures 3a, 3d, 3e and 12a, S17a, S17b and S17c in Supporting Information S1) and show no evidence of significant crystal-plastic deformation (Figures 5a–5d).

Garnet and kyanite are concentrated adjacent to large garnet grains at the pseudotachylyte boundary and show a streaming away from this source consistent with a dextral sense of shear (Figure S17 in Supporting Information S1). Small kyanite needles are well-aligned parallel to the planar feldspathic compositional layering. The cauliflower garnet overgrows this planar fabric but is also commonly aligned in straight compositional trains that make a larger angle to the pseudotachylyte layer walls than the foliation defined by feldspar and kyanite (Figures 12a, S17 in Supporting Information S1). The aligned kyanite shape fabric does not bend around

**Figure 8.** Back-Scattered Electron (BSE) image and Electron Backscatter Diffraction (EBSD) maps of a large relict garnet grain bordering the pseudotachylyte layer in AW9B_1a. For location see Figure 2f. (a) BSE image. (b) EBSD phase + IQ map. Note the prominent quartz inclusion (1) protruding into the pseudotachylyte and the inclusion (2) located between two fractures and shattered on its right side in the area of fracture intersection. Note also the magnetite present along some fracture surfaces. (c) EBSD IPF + IQ map for garnet and quartz (hexagonal). Note the slight progressive variation in crystallographic orientation of inclusion (1), reflecting minor dextral shear in the pseudotachylyte. Note also the zone of new quartz grains at the right side of inclusion (2). The step size in (b) and (c) is 1.73 μm, resulting in 963,264 data points.

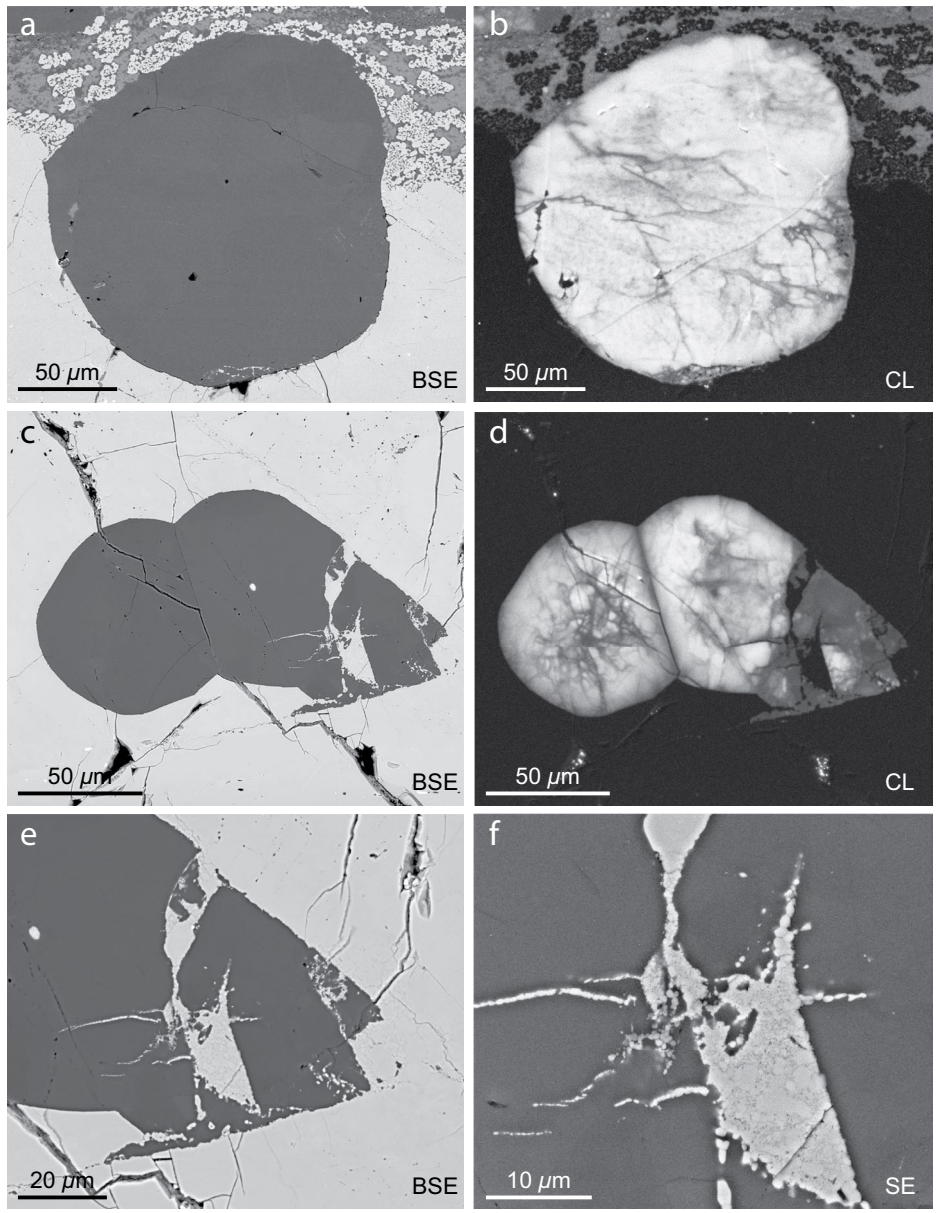


**Figure 9.** Scanning electron microscope images showing details of the quartz inclusions (1) and (2) from Figure 8. (a) Back-Scattered Electron (BSE) image of inclusion (1). Note that it protrudes into the pseudotachylyte layer and is wrapped around by trains of new cauliflower garnet grains crystallized from this flowing melt. Flow has resulted in minor dextral shear of the protruding part of the inclusion. (b) Cathode-Luminescence (CL) image of inclusion (1). A limited number of dark lines interpreted as healed microfractures are parallel to the boundary of the pseudotachylyte and to the main set B fracture in the large garnet (Figure 8). (c) BSE image of inclusion (2) showing the dilatant extensional fracture now filled with pulverized garnet. (d) CL image of the same area. Note that the shattered right side of the inclusion is also darker in CL. (e) BSE image of right side of (c). (f) SE image of the pulverized garnet filling the dilatant fracture. Note the wide range of sizes and irregular shapes within the main fracture and dodecahedral shapes of more constant size in the garnet apophyses and veins.

the cauliflower garnet and is locally overgrown. Kyanite is also present in the pseudotachylyte injection veins (Figure 12f), where it is generally well-aligned and locally forms "log-jam" structures where the vein narrows.

Magnetite and hematite are generally absent in the areas of new garnet growth (Figure S17 in Supporting Information S1). Minor amounts of biotite are present in the granulite host rock and are expected to have readily melted during the frictional event (Bestmann et al., 2011; Papa et al., 2021). Biotite is locally observed in the pseudotachylyte in minor amounts as small circular spherulites (e.g., Figure S9a in Supporting Information S1).

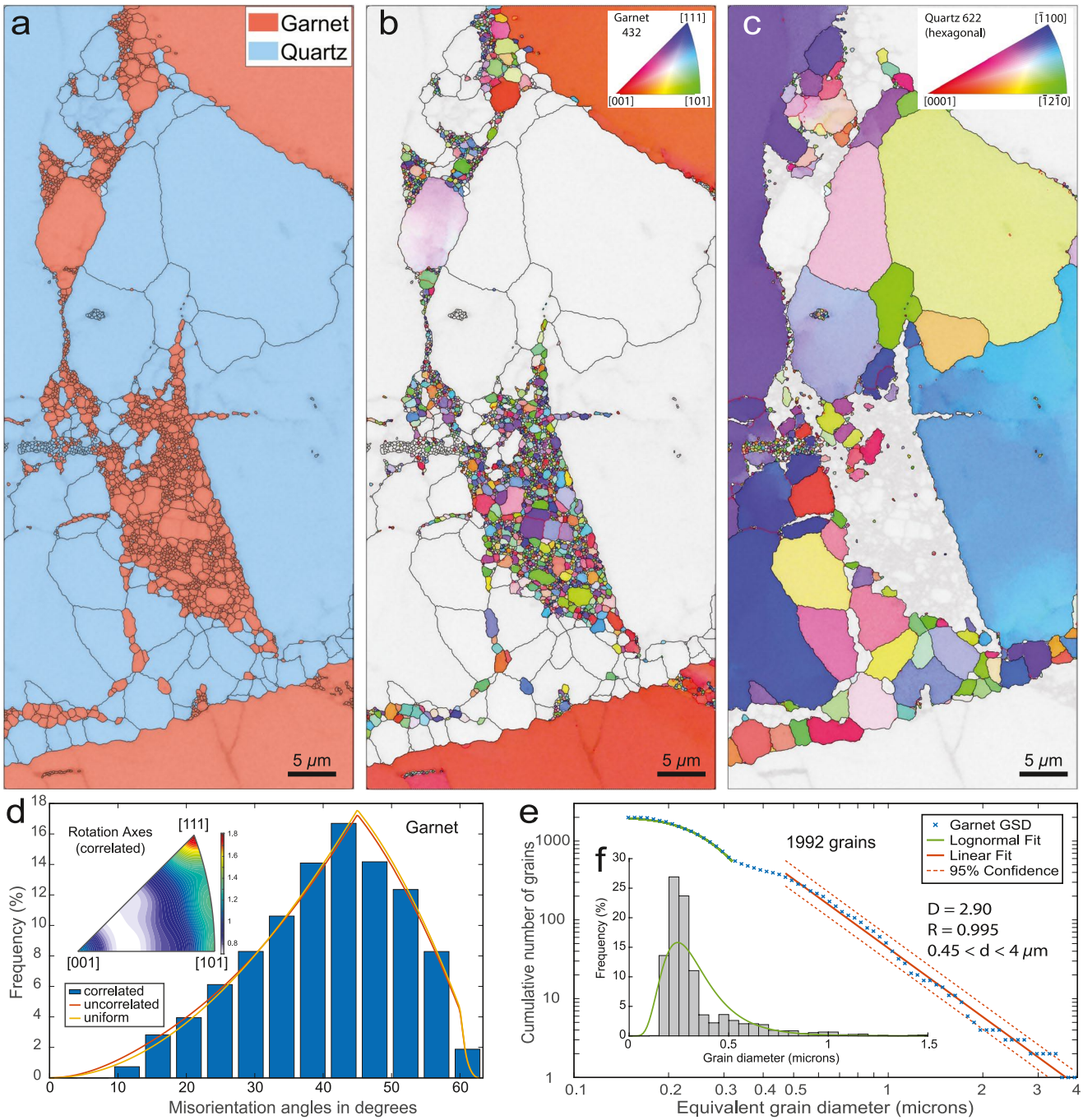


**Figure 10.** Electron Backscatter Diffraction (EBSD) and Grain Size Distribution (GSD) analyses of the area of inclusion (2) in Figure 9e. (a) EBSD phase + IQ map. (b) EBSD IPF + IQ map for garnet. (c) EBSD IPF orientation map for quartz (hexagonal). The step size in (a)–(c) is 0.087 μm, resulting in 252,360 data points. (d) Misorientation angle plot for grains with $d < 30$ μm; inset shows the rotation axes for the correlated (neighboring) grains (4,436 pairs), which shows a weak preference for [111]. (e) Log-log plot of the GSD for garnet with $d \leq 4$ μm. (f) Histogram of relative frequency of garnet grain sizes (linear scale) with best-fit lognormal distribution indicated.

## 5. Discussion

Fracture sets A and B show no evidence of reactivation. Recrystallized grains along fractures crossing quartz ribbons (Figure 4) were not later refractured and grain boundaries remained tight. Dilated grain boundaries in fractures across feldspar are commonly bridged by fibrous materials linking matching sides and outlining the

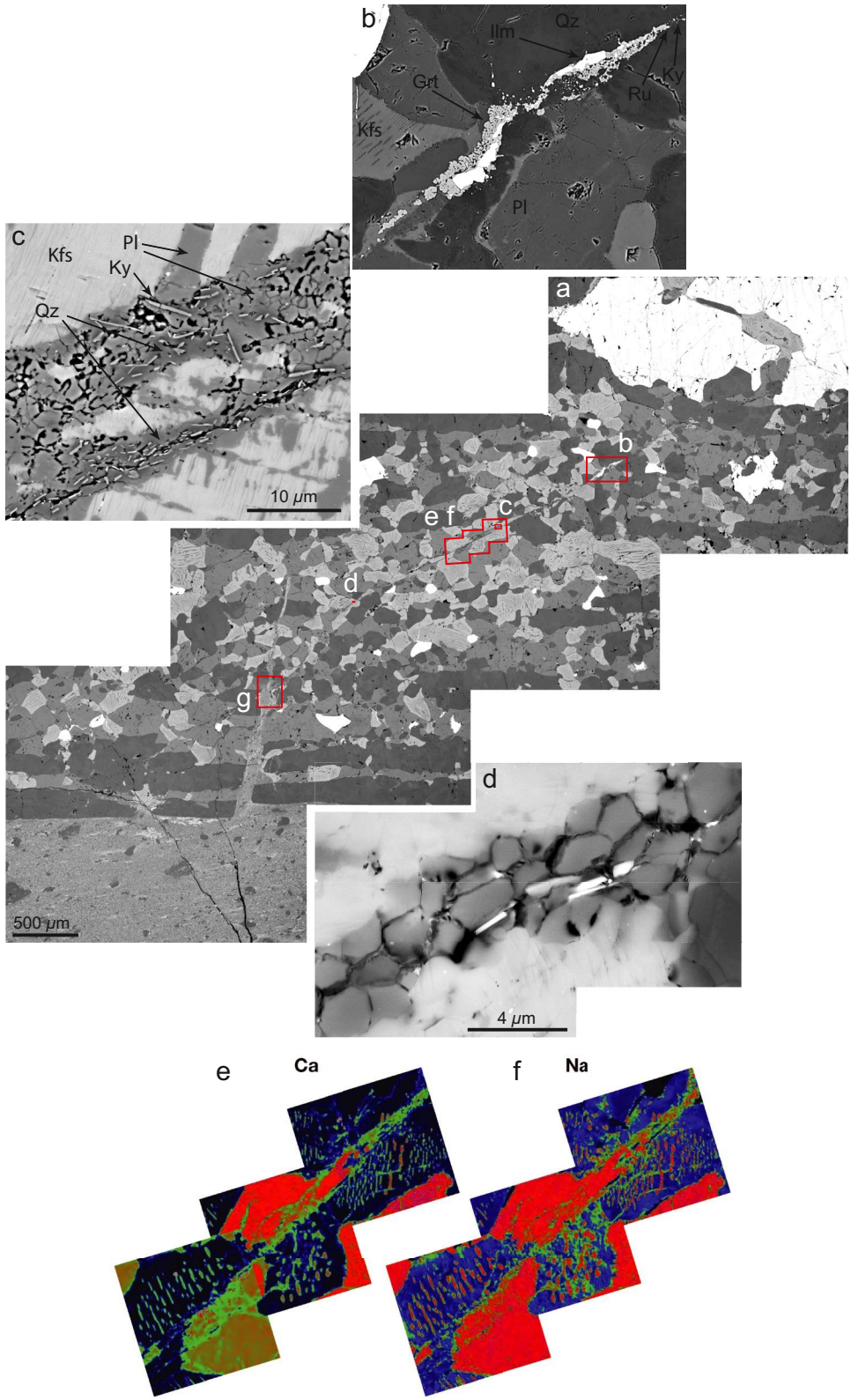
b
Ilm
Qz
Grt
Ky
Ru
Kfs
Pl
c
Kfs
Pl
Ky
Qz
10 μm
a
b
e f
c
d
g
500 μm
d
4 μm
e
Ca
f
Na

**Figure 11.**

opening direction of the dominantly tensile fractures (Figures 11d, S16d in Supporting Information S1). If the fractures of sets A and B preceded the pseudotachylyte-generating faulting, then they should have been reactivated during the earthquake event, but this is not observed. We therefore infer that the host rock fracturing, asymmetrically developed to either side of the main pseudotachylyte and crosscut by the pseudotachylyte injection veins, was coseismic with the pseudotachylyte-generating rupture.

From crosscutting relationships, a sequence of coseismic events that occurred during a single earthquake can be established (Figure 13):

1. dynamic, asymmetric fracturing in the damage zone during initial rupture propagation; healing of these microfractures predated (2) and (3)
2. frictional wear, rapid heating, and thermal-shock fracturing
3. friction-induced melting (pseudotachylyte formation) and melt injection
4. ductile shearing of melt, which continued during melt cooling and crystallization

The granulite facies host rock contains very minor amounts of biotite (the only hydrous mineral). There is no evidence for infiltration of hydrous fluids related to enhanced permeability induced by the seismic fracturing, in contrast to otherwise comparable examples from the Bergen Arcs, Norway (Austrheim, 1987; Jamtveit et al., 1990; Jamtveit, Moulas, et al., 2018; Kaatz et al., 2021). Solid-state, ductile shearing of the pseudotachylyte layer (stage 6 in Figure 13) is absent as demonstrated by the lack of significant crystal-plastic deformation of quartz clasts within the pseudotachylyte. Hydration associated with fluid infiltration during exhumation is also absent. The textures very much resemble the dry pseudotachylyte from the mantle peridotite of the Lanzo massif in the western Alps (Pennacchioni et al., 2020) that escaped hydration and ductile deformation in the eclogite-facies subduction environment and throughout the exhumation path to the surface.

Although the AW9 pseudotachylyte did not localize subsequent solid-state ductile shear, other samples from the surrounding region do show cycles of seismic fracturing and melting followed by aseismic high-temperature shearing. This would be consistent with localized weakening of the dry lower crustal rocks as a result of seismic fracture and associated grain size reduction (Hawemann, Mancktelow, Pennacchioni, et al., 2019; Hawemann et al., 2018; Jamtveit, Ben-Zion et al., 2018; Wex et al., 2017, 2019).

In the sketch of Figure 13, initial seismic rupture (stage 1) is associated with off-plane fracturing flanking a propagating fault tip. The fracture sets A and B are related to the fault surface, now outlined by the pseudotachylyte, and fade away from the fault (Figures 1, 2 and 13). Pulverization and injection of garnet powder (GSD with D-value of 2.9) are locally developed along fractures (Figure 10) and provide evidence that the off-plane fractures developed dynamically during earthquake rupture (Incel et al., 2019; Reches & Dewers, 2005; B. R. Song et al., 2020). The similarity to fractures developed in the experiments of Trepmann et al. (2007), simulating mid-crustal coseismic deformation of quartz, also supports this interpretation. The new quartz grains along such fractures, with a random CPO, were interpreted by Trepmann et al. (2007, 2017) to develop by rapid stress relaxation after earthquake rupture below the usual seismogenic zone. Strong kinking of host-rock biotite, observed throughout the AW9 thin sections, has been reported adjacent to other pseudotachylyte veins (e.g., Passchier, 1982) and interpreted to be characteristic of coseismic deformation (Anderson et al., 2021; Bestmann et al., 2011; Di Toro & Pennacchioni, 2005).

Earthquake rupture tip propagation is retarded by the energy consumed in microfracturing (e.g., Andrews, 2005; Suzuki, 2012; Yamashita, 2000), but still occurs at a sub-Rayleigh wave velocity (e.g., Reches & Dewers, 2005; Suzuki, 2012) on the order of km/s. In contrast, frictional slip on the developed main rupture surface, causing wear (stage 2) and melting (stage 3), will be on the order of m/s (Petley-Ragan et al., 2019). This is reflected in the

**Figure 11.** Scanning electron microscope images and Electron Micro-Probe Analysis (EMPA) chemical maps from a continuous fracture of set A in AW9B_2b. For location, see Figure 2c. (a) Overview Back-Scattered Electron (BSE) mosaic. Note that the pseudotachylyte injection vein, which is ca. perpendicular to the main pseudotachylyte, crosscuts this fracture without diversion. (b) New growth of plagioclase, quartz, cauliflower garnet, ilmenite, rutile, and kyanite along the fracture. For EMPA analyses of the minerals, see Table S1 in Supporting Information S1. (c) BSE image showing growth of new plagioclase (An 21–25), quartz, and kyanite fibers. Note the currently pervasive open porosity. (d) BSE image at higher magnification showing currently open grain boundaries to newly grown plagioclase, $SiO_2$-rich (darker) grain boundary films and fibers linking matching boundaries. Note also the growth of kyanite fibers across these currently open boundaries. (e) and (f) Chemical maps showing the relative enrichment of Ca and Na along the fracture, reflecting the growth of new plagioclase with An ca. 21–25. Red colors are higher concentrations, green intermediate and blue lower. Note in (e) that this new plagioclase is more albitic (lower Ca) than the original relict large plagioclase grains. (g) Location of chemical maps presented in Figure S14 in Supporting Information S1.

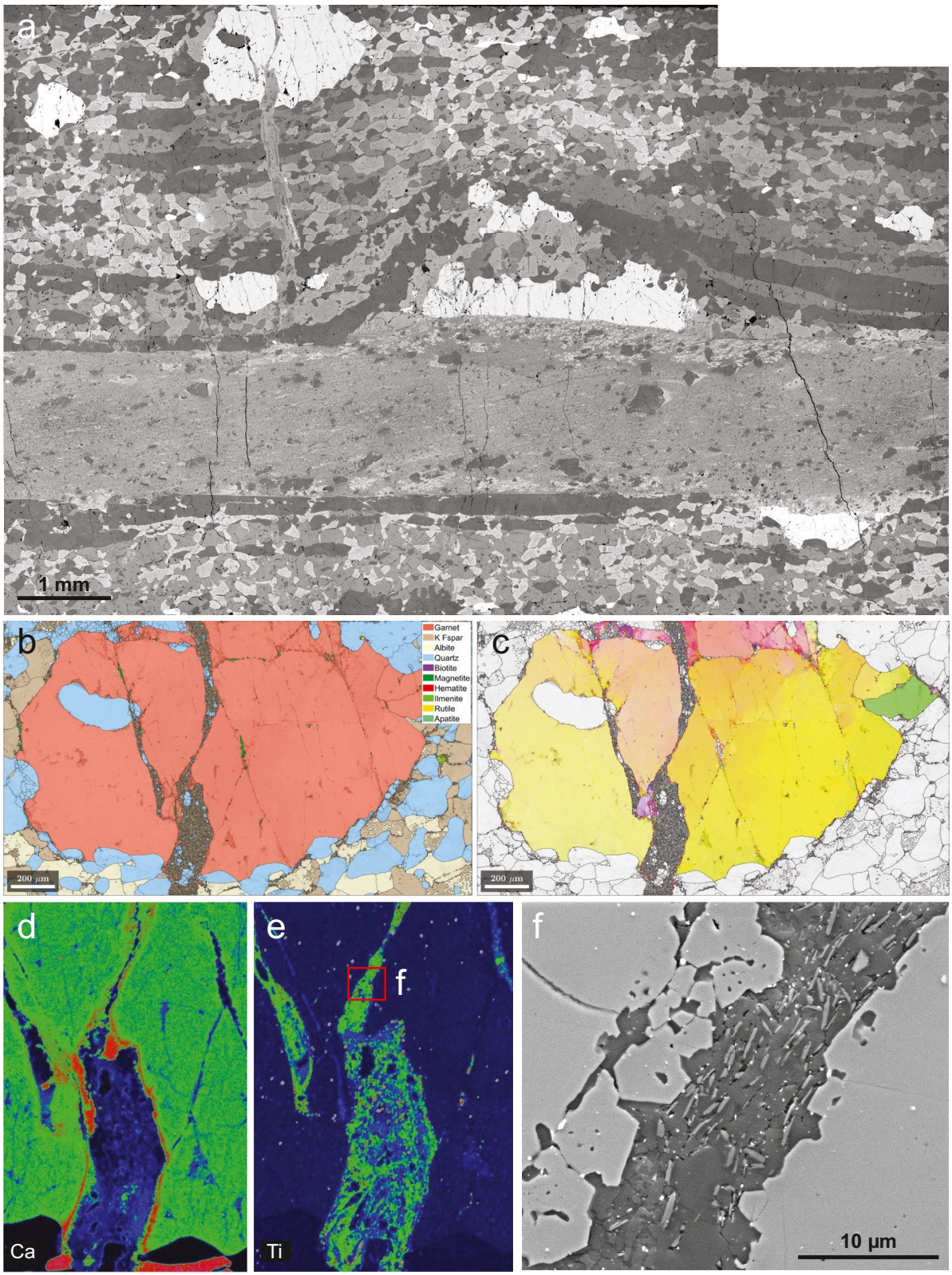
a
1 mm
b
Garnet
K Fspar
Albite
Quartz
Biotite
Magnetite
Hematite
Ilmenite
Rutile
Apatite
200 μm
c
200 μm
d
Ca
e
f
Ti
f
10 μm

**Figure 12.**

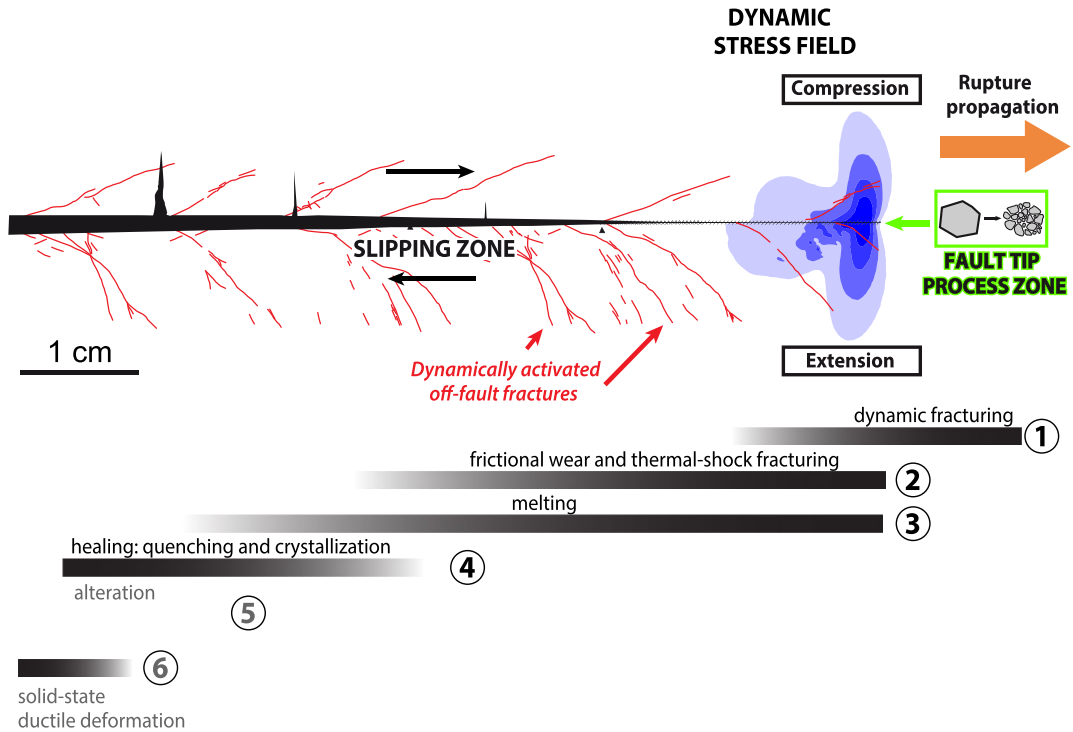


**Figure 13.** Cartoon summarizing the temporal evolution of deformation processes related to seismic rupture. Redrawn and modified after Swanson (1992), Rice et al. (2005), Di Toro et al. (2009), Petley-Ragan et al. (2019), and Okubo et al. (2019). Contours at the fault tip indicate particle velocity magnitude following Okubo et al. (2019), giving an indication of the distribution of the propagating process zone at the rupture tip, and the compressional and extensional sides, from Figure 3 of that publication.

observation that frictional melting on the main fault postdates the pervasive microfracturing (e.g., Figure 3) and formation of the secondary fractures of sets A and B. Healing of the host rock fractures also occurred before the stage of frictional melt production since healed cracks are preserved within quartz clasts in the pseudotachylyte (Figure 5) and pseudotachylyte injection veins crosscut host rock fractures without diverging or following these earlier cracks (Figure 11).

The microfractures of sets A and B have minor shear offset and are predominantly tensile (mode I) fractures. The matching geometry of opened grain boundaries with connecting, nearly orthogonal fibers (Figures 11d, S16d in Supporting Information S1) also demonstrates that the fractures were mainly tensile. Tensile fractures develop for small effective confining pressure and differential stress. Considering the Griffith/Navier-Coulomb brittle failure envelope, a material with tensile strength $T$, maximum principal compressive stress $\sigma_1$, minimum principal compressive stress $\sigma_3$, and pore fluid $p$ (e.g., Price & Cosgrove, 1990):

1. tensile failure occurs when $(\sigma_3 - p) = -T$ and $(\sigma_1 - \sigma_3) < 4T$
2. hybrid, mixed mode I + II if $-T < (\sigma_3 - p) < -0.8T$ and $4T < (\sigma_1 - \sigma_3) < 5.5T$
3. otherwise, failure is in shear (mode II)

The tensile strength of quartz is ca. 150 MPa (Chao & Parker, 1983), similar to that for the San Marcos gabbro with 68% plagioclase (Ai & Ahrens, 2004). Using this value, the maximum differential stress for tensile failure

**Figure 12.** Electron Backscatter images, Electron Backscatter Diffraction (EBSD) maps, and Electron Micro-Probe Analysis chemical maps related to a pseudotachylyte injection vein in AW9B_2b. For location, see Figure 2c. (a) Back-Scattered Electron (BSE) overview mosaic. (b) EBSD phase + IQ map of the large garnet in the uppermost left area. (c) EBSD IPF + IQ map for this garnet. The step size in (b) and (c) is 1.73 µm, resulting in 762,700 data points. (d) Chemical map for Ca from the lower central part of (b) and (c). Red colors are higher concentrations, green intermediate and blue lower. (e) Chemical map for Ti from the lower central part of (b). Red colors are higher concentrations, green intermediate, and blue lower. (f) BSE image showing the flow pattern outlined by kyanite fibers. Location is indicated in (e).

in a quartzo-feldspathic rock, such as AW9, is ca. 600 MPa. For a thrusting regime, appropriate to the hanging wall of the Woodroffe Thrust, $\sigma_3$ is vertical and equal to the lithostatic load. Assuming that the metamorphic pressure of ca. 1.2 GPa corresponds to lithostatic load, the minimum pressure reduction to cause tensile failure is ca. 1.35 GPa with effective pressure at failure <650 MPa. The syn-tectonic mineral assemblage of sample AW9 demonstrates that the system was water-absent, although other fluids, for example, $N_2$ or $CO_2$, could have been present (Andersen et al., 1993; Larsen et al., 1998). However, for the extremely fast seismic deformation rates, the rock is effectively an "undrained" system with a consequent strong effect of "dilatancy hardening" (Brace & Martin, 1968; Brantut, 2020; Frank, 1965, 1966; Paterson, 1978; Rice et al., 2005). There is therefore a negative feedback effect that argues against high pore fluid pressure as a significant contributory factor for tensile fracture in these lower crustal rocks. It follows that tensile fracturing under ambient pressure of ca. 1.2 GPa was only possible during seismic decompression of ca. 1.35 GPa associated with the propagation of the fault tip (Figure 13). This is compatible with the extreme mechanical conditions (tensile stresses approaching 5 GPa and volumetric strain rates exceeding $10^5$ $s^{-1}$) estimated by Reches and Dewers (2005) near an earthquake rupture tip propagating at close to the Rayleigh shear wave velocity.

Dynamic underpressure can explain the tensile fractures on the extensional side of the fault tip (set B for the geometry of Figure 13) as predicted in numerical models (Di Toro, Nielsen, & Pennacchioni, 2005; Okubo et al., 2019). However, these models do not predict the set A on the compressional side. Limited fractures with the orientation of set A are also observed on the side dominated by set B (Figure S15 in Supporting Information S1). The presence of both fracture sets on both fault sides is, however, well explained by the elastic model of Reches and Dewers (2005). This model predicts very dynamic fluctuation of stresses on both sides of the rupture, which changes from volumetric expansion to volumetric contraction during the few microseconds of passage of the earthquake rupture. This further supports the interpretation that the host rock fracturing associated with the AW9 pseudotachylyte is coseismic. The fluctuation in volumetric strain rates predicted by Reches and Dewers (2005) has not previously been documented in a natural example.

The newly grown anhydrous metamorphic assemblage along fractures and opened grain boundaries is consistent with the ambient Petermann conditions (i.e., ca. 650°C, 1.2 GPa) and is commonly associated with markedly, increased porosity (Figures 11c, 11d, S15 and S16 in Supporting Information S1). Bridging kyanite needles (Figures 11d, S16d in Supporting Information S1) indicate that dilation was coeval with kyanite growth. The locally preserved, $SiO_2$-enriched material filling the porosity (e.g., Figures 11d, S15b, S15c, S16c and S16d in Supporting Information S1) shows fibers that track the tensile opening direction of matching sides of the cracks or grain boundaries during growth. If the tensile cracks were seismic, the fibers formed in microseconds during catastrophic extensional opening of boundaries at very low (<650 MPa) or potentially negative effective pressure. Under these extreme conditions, the fibrous material was quite likely amorphous (Hayward et al., 2016) and considering the anhydrous conditions and general degree of preservation of fine microstructure, it may have remained amorphous (Dunkel et al., 2021; Pennacchioni et al., 2020). The dilatant grain boundaries were probably originally completely filled by such fibrous, amorphous material, and the observed associated porosity results from later etching, possibly during sample preparation.

The trace of set A and B fractures is typically marked by a zone of new grains or by epitaxial healing. Similar to the experiments of Trepmann et al. (2007) aimed at replicating coseismic processes, newly grown quartz grains along microfractures have a random CPO. There is no evidence for progressive subgrain rotation, although subgrains with a size similar to the new grains are observed in the host quartz ribbon (Figure 4d). Lobate grain boundaries typical of fast grain boundary migration are not observed. Aggregates of annealed polygonal grains are also not observed, despite the high ambient temperature of ca. 650°C. The GSD for the quartz new grains is well-fitted by a continuous gamma or Weibull function, although for the majority of grains with $d < 20$ µm, a lognormal fit is equally good (Figures 4g and 4h).

The GSD and CSD are critical data for assessing the mechanisms of recrystallization, new grain growth and annealing versus cataclasis, grinding, and pulverization. Lognormal and gamma distributions, as found for quartz new grains along the fractures, are reported for newly grown or recrystallized grains from a wide range of materials and conditions. Qualitatively, the grain size histograms for recrystallized quartz in Figure 3 of Cross et al. (2017) are lognormal, as was also found by Okudaira et al. (2013) in metacherts from a contact aureole. For olivine, a lognormal GSD was reported by Tasaka et al. (2016) both for samples produced by hot pressing and for deformed samples from torsion experiments. Aupart et al. (2018) reported a power law GSD for olivine from

a wide range of both experimentally and naturally deformed samples. However, lognormal distributions were found for high-temperature experiments and some mantle-deformed natural samples, where grain growth could be important.

A continuous lognormal (or gamma or Weibull) distribution is in itself not characteristic of grain growth and is often used to approximate the PSD of pulverized material or when solid materials are exposed to long-term mechanical comminution (Neikov & Yefimov, 2019). Fowler and Scheu (2016) measured the PSD resulting from laboratory decompression explosions of volcanic rock, which can be approximately represented by gamma distributions. Phillips and Williams (2021) recently critically reassessed PSD data from a wide range of natural and experimental fault rocks and concluded that lognormal distributions are the best description in a majority of the cases.

Quartz clasts in the pseudotachylyte show an internal microstructure identical to that of quartz in the damaged host rock. Large portions of the clasts consist of fragments of nearly undeformed monocrystalline ribbon grains with local healed microfractures (Figure 5b). The clasts show no evidence for significant crystal-plastic deformation or pervasive recrystallization prior to melting. Irregular planar zones of newly grown quartz grains (Figure 5d) are directly comparable to zones of new grain growth marking healed fractures in the host rock (Figure 4). As in the host rock, the CPO of these new grains is random (Figure 5f). The GOS of the new grains is distinctly lower than that for the large grains of the relict host (Figure 5e) as also observed in the country rock (Figures S5a and S6e in Supporting Information S1). Smaller grains within the pseudotachylyte are either single or composite grains with a similar shape and size distribution to that of recrystallized quartz within the larger grain in Figure 5. The recrystallized grain size within the clast is, if anything, slightly smaller than that of new quartz grains in the host rock (Figure 5h), so there is no suggestion that the envelopment in pseudotachylyte melt promoted grain growth or annealing. The CL signature of the newly crystallized grains, both in the limited zones within the large clast of Figure 5b and in the smaller clasts, is darker than the relict material, similar to what is observed on more discrete healed microfractures in the host rock. Overall, the observations indicate that microfracturing, healing, and new grain growth occurred before clast formation. This implies that growth of 20–30 μm-sized new grains occurred in microseconds between the fault tip propagation and off-fault damage zone development, and on-fault cataclasis, wear, and frictional melting.

In contrast to the quartz new grains, the CSD of amalgamated quartz clasts shows a more linear distribution on a log-log plot with a D-value of 1.7. This value is the same as the most common one obtained by Di Toro and Pennacchioni (2005) for pseudotachylytes in the Adamello batholith of the Southern Alps, but the corresponding arithmetic mean grain size of 3.9 μm is markedly smaller than that in their examples (see their Figure 10).

In contrast to quartz, feldspar shows a composite GSD. For small grain sizes <5 μm, a lognormal distribution is the best fit. This is consistent with the microstructural observation that these are newly grown grains, with the new plagioclase not only recrystallizing but also growing in relict K-feldspar and vice versa (Figure 4c). As with quartz, the CPO of these feldspar grains, dominated by the much larger number of small grains, is random (Figures 6c and 6d). As observed in other studies (e.g., Mancktelow & Pennacchioni, 2004), the grain size of recrystallized or newly grown feldspar is significantly smaller (<5 μm) than that of quartz (<30 μm). The much lesser number of larger "grains" represent fractured clasts of the original large relict grains and show a linear GSD distribution on the log-log plot with a D-value of 1.67 (for combined plagioclase and K-feldspar; Figure S10 in Supporting Information S1). This value is identical to that obtained for quartz clasts within the pseudotachylyte (Figure S9f in Supporting Information S1).

Garnet shows a GSD pattern similar to that of feldspar but with a cutoff between a lognormal and linear distribution at ca. 2 μm (Figure 7k). Consequently, more of the grains probably correspond to clasts. Although the CPO is still random (Figure 7j), correlated grains show a tendency to lower misorientation and rotation around the crystallographic axes [111] and [101] (Figure 7i). This was also found by Hawemann, Mancktelow, Pennacchioni, et al. (2019), together with TEM evidence for the interplay between fracturing and crystal-plastic processes in garnet. The D-value is consistently higher (2.59 when data from all measurements are combined, Figure S13a in Supporting Information S1) than in feldspar. The D-value is toward the upper limit of the values obtained by B. R. Song et al. (2020) for garnet from the core of the Sandhill Corner shear zone. Such high values are interpreted by B. R. Song et al. (2020) to be characteristic for dynamic fragmentation during rupture propagation as also considered to be the case in the current sample.

An example of injection of cataclastic material is provided by the quartz inclusion within the garnet of Figures 8, 9, and 10. The intersection of two fractures in the host garnet (Figures 8b and 8c, S11, S12 in Supporting Information S1) resulted in a dilational pull-apart within the quartz inclusion filled with garnet powder (Figures 9, 10). Powder expulsion from the coseismic slipping surface is observed during the initial stages of high velocity experiments in rotary rigs that simulate seismic slip (Niemeijer et al., 2011). To date, pulverization has been reported from experiments (Incel et al., 2019) and pseudotachylyte-bearing rocks (Austrheim et al., 2017; Jamtveit et al., 2019; Papa et al., 2018; Pennacchioni et al., 2020; Petley-Ragan et al., 2018, 2019; Trepmann & Stockhert, 2002) and interpreted as in-situ shattering related to the dynamic stress field during earthquake rupture propagation.

The pulverized garnet is identical in composition to the surrounding host garnet (Table S1 in Supporting Information S1). It has a random distribution, an RMS grain size of 0.45 ± 0.28 μm, and a high D-value of 2.9. The injected powder escaped significant grain growth or annealing (Figure 9), despite the very fine grain size and the high-grade metamorphic conditions. Only the grain shape shows modification toward a polygonal shape (e.g., Figure 9f). Injection must have been instantaneous during coseismic dilational fracturing of the quartz inclusion.

Mechanical introduction of pulverized material could also explain the occurrence along fractures of new minerals with different composition to the immediate host. As outlined in Sections 4.6 and 4.7, the fractures and related zone of chemical alteration, with new mineral growth, are crosscut by pseudotachylyte injection veins. This implies that fracturing and introduction of the material were effectively synchronous and nearly instantaneous. As in the quartz inclusion, the foreign material could be injected as a cataclastic powder along transiently dilational fractures. Growth of new minerals from this introduced powder occurred subsequently under the ambient high-grade conditions. The lack of growth of these new minerals into or across pseudotachylyte injection veins suggests that this mineral growth may also have occurred in the very short time between fracture formation and injection of the pseudotachylyte.

Features related to stage (2) of frictional wear and possible thermal-shock fracturing are largely obscured by subsequent frictional melting. Embayments of pseudotachylyte into large garnets and the protruding quartz inclusion (1) of Figure 8 demonstrate that the melt zone widened beyond the precursor fault zone with the result that details from within this zone are now lost. However, the similarity in the microstructure of the quartz clasts to that of the relict quartz ribbon grains in the host rock, together with the total lack of evidence for precursor (ultra-) mylonitization, indicates that melting was not preceded by extreme crystal-plastic deformation and self-localizing thermal runaway (John et al., 2009; Kelemen & Hirth, 2007; Papa et al., 2020; Thielmann, 2018; Thielmann et al., 2015).

In the pseudotachylyte of AW9, which developed in a quartzo-feldspathic host rock, clasts only consist of quartz. However, in the literature, pseudotachylytes within feldspar-bearing rocks invariably contain feldspar clasts (Austrheim & Boundy, 1994; Camacho et al., 1995; Di Toro & Pennacchioni, 2004; Maddock, 1983; Passchier, 1982; Pittarello et al., 2012; Sarkar et al., 2019; Sibson, 1975; Spray, 1992; Steltenpohl et al., 2006; Wenk & Weiss, 1982). These observations suggest a friction-induced temperature high enough to melt all minerals except quartz. As discussed in Papa et al. (2021), the non-equilibrium melting temperature of minerals during pseudotachylyte development is not well known, but estimates have been made (e.g., Spray, 2010; Papa et al., 2021): plagioclase (An 35) likely begins incongruent melting at ∼1200°C and reaches the liquidus at ∼1400°C, whereas quartz melts at 1715°C, although Lee et al. (2017) proposed frictional melting of quartz at lower temperatures (1350–1500°C). Qualitatively, the lack of feldspar clasts implies that the AW9 pseudotachylyte melt attained an unusually high temperature, suggesting a relatively energetic seismic event for its small size.

Pseudotachylyte injections, only observed on one side of the main fault vein (Figure 1), remain relatively straight and perpendicular to the fault, even where crosscutting set A fractures (Figures 1, 2 and 11a) and large garnets (Figure 12a). The tensile fracture sets A and B are asymmetrically arranged at an angle to the main fault, indicating that they formed when a significant shear stress was maintained on the main fault during dynamic rupture propagation. The primary orientation of $\sigma_1$ was ca. parallel to set B (i.e., about 60° to the fault surface), consistent with the angle predicted for dynamic off-fault structures by Okubo et al. (2019). As the fault tip moved away, the shear stress decreased with slip, cataclasis, increase in temperature and, especially, development of melt. By the time of melt injection, shear stress on the layer was very low and the principal stress axes would have rotated adjacent to the pseudotachylyte. Because the primary angle to $\sigma_1$ was greater than 45°, this rotation would result in $\sigma_1$

being nearly perpendicular and $\sigma_3$ nearly parallel to the melt-filled fault. The rotated orientation of the principal stress axes then controlled the development of nearly perpendicular tensile injection veins produced during the stage of frictional coseismic slip. This proposal contrasts with the interpretation for the injection veins described from the Gole Large Fault Zone in the Adamello intrusion by Di Toro, Nielsen, and Pennacchioni (2005), who inferred that injection veins fill fractures developed during the propagation of the earthquake rupture tip. During extension of layered materials, the relative dynamic pressure should be higher in the weaker layer with the difference in magnitude scaling with the strength of the strong layer (Mancktelow, 2008). This aides the development of tensile injection veins by both increasing the fluid pressure in the injecting melt and reducing the effective pressure in the host rock, promoting tensile rather than shear failure (Zhong et al., 2021).

In Figures 12b and 12c, the injection vein enters the garnet without diversion, ca. perpendicular to $\sigma_3$ and parallel to $\sigma_1$. Within the garnet, the vein bifurcates to follow a set of conjugate fractures developed symmetrically about $\sigma_1$ with an apparent opening angle of ca. 40°. If these fractures intersect in the line perpendicular to the interpreted movement direction (Figure 1), the true opening angle should be ca. 30°. Displacement on these fractures is not discernible and they are effectively "shear joints", presumably mixed mode I + II fractures. The cohesion of garnet is much greater than that of quartz or feldspar (Incel et al., 2019; Kavner, 2007; Pardavi-Horváth, 1984). For the same differential stress, tensile fracture driven by a decrease in effective confining pressure is promoted relative to mixed mode or shear failure in materials with higher cohesion. Reduction in effective confining stress may be due to continued dynamic pressure reduction, to the pore-fluid effect of the injecting melt vein, or both. At the time of vein injection, deformation was driven by displacement (or velocity) boundary conditions related to the seismic event and stresses were higher in the garnet with the extension accommodated by conjugate mixed-mode rather than tensile fracturing as occurred in the quartz and feldspar layers.

The melt foliation in the main pseudotachylyte fault vein is defined by compositional heterogeneity of the feldspar matrix and the shape-preferred orientation of kyanite needles. Garnet growth occurred relatively late in the crystallization sequence, crosscutting the flow layering in feldspar and the aligned kyanite, but still developing a foliation during continued flow in the pseudotachylyte as it crystallized. Both the shape and compositional fabrics are planar, implying almost constant viscosity of the pseudotachylyte melt across the fault vein width during progressive melt crystallization and growth of garnet. Crystallization must have occurred in the very initial, high-temperature stages of cooling before quenching at the borders of the pseudotachylyte layer established a temperature gradient. This gradient should result in localization of strain toward the hotter, less viscous vein center, which is not observed. Ductile shear flow did not continue in the totally solidified pseudotachylyte as indicated by the lack of significant crystal plastic deformation and elongation of the quartz clasts.

## 6. Conclusions

The studied sample exceptionally preserves the sequence of structures developed during a single seismic event in the lower continental crust, below the depth of the usual brittle-ductile transition, which is generally taken to mark the base of the seismogenic zone. However, the similarity of the CSD between fractured clasts in the pseudotachylyte and in the host rock, both with a D-value of ca. 1.7, as well as the identical microstructure within quartz clasts in the pseudotachylyte and the quartz ribbons of the host rock, is strong evidence for brittle failure during earthquake rupture and frictional heating during slip, leading to eventual melting. There is no evidence for strongly localized crystal-plastic shear and mylonitization as a precursor to melting as should be expected for a thermal runaway process. Therefore, we conclude that this lower crustal earthquake developed by a brittle-frictional mechanism similar to that for shallow earthquakes. The microstructural sequence records the development of the initial seismic rupture and the associated localized damage zone developed asymmetrically at the propagating crack tip, localized pulverization and extremely rapid new grain growth on these off-fault, predominantly tensile, fractures, slip accumulation and eventual melting on the main rupture, and finally quenching and solidification of the melt as it returned to ambient temperatures. This provides a rather unique time-lapse record that can be used to constrain the mechanisms of earthquake rupture and pseudotachylyte development on the micron to centimeter scale of the current observations.

There is no evidence for any significant infiltration of hydrous fluids during or subsequent to this seismic event. The introduction of new material along discrete fractures cannot have been facilitated by high pore fluid pressures or fluid-enhanced diffusion. Instead, it is concluded that foreign material was nearly instantaneously introduced

through injection of pulverized material along the transiently dilatant tensile microfractures. A direct model for this is provided by the example of pulverized garnet that filled an adjacent dilatant fracture in a large quartz inclusion within a garnet host. This proposal provides an explanation for the growth of new, compositionally different minerals (e.g., quartz, feldspar, kyanite, magnetite, ilmenite, garnet, and rutile) observed along healed fractures. This new mineral growth, and the associated compositional change, is apparently crosscut by pseudotachylyte injection veins, with the conclusion that this mineral growth occurred during the earthquake. Growth of new grains of random quartz and feldspar along fractures is also interpreted to have happened during the earthquake. Quartz clasts in the pseudotachylyte show the same microstructure of new grains outlining healed fractures that is documented in the damage zone in the flanking country rock. These new grains have also been disaggregated into the pseudotachylyte melt. The new quartz grain growth must therefore have occurred in seconds between fracture formation in the damage zone of the propagating crack and incorporation of the clasts into the developing pseudotachylyte melt. Thermal effects due to envelopment in the pseudotachylyte have not modified either this microstructure or the fine-scale structure of healed microfractures visible with CL. The remarkable conclusion is that the growth of new grains of quartz and feldspar, and locally also the growth of new minerals, occurred in a very short time on the order of microseconds to seconds, but then remained unmodified, even down to the submicron scale, for hundreds of millions of years. Features, such as the asymmetric development of tensile fractures and localized pulverization under lower crustal conditions, reflect a very dynamic and extreme variation of stress in space and time, which is characteristic of a propagating earthquake rupture.

## Data Availability Statement

EBSD and grain size data as well as high-resolution figures are publicly available at http://doi.org/10.25430/researchdata.cab.unipd.it.00000516.

**Acknowledgments**
Constructive and thorough reviews by Elena Miranda and an anonymous reviewer, as well as by Isabelle Manighetti and an Associate Editor of JGR, are gratefully acknowledged. We thank the communities of the Anangu Pitjantjatjara Yankunytjatjara Lands (APY) for granting access to the Musgrave Ranges. We also gratefully acknowledge the support of Luiz Morales and Karsten Kunze and the Scientific Center for Optical and Electron Microscopy (ScopeM) of the ETH Zurich for use of equipment (SEM and EBSD), scientific support, and discussions. Luiz Morales, Rüdiger Kilian, and Ralf Hielscher provided support during modification of MTEX scripts for the EBSD analysis. Friedrich Hawemann and Sebastian Wex are thanked for their contributions as part of the team in the Musgrave Ranges during their PhD work. Funding from the University of Padova and PRIN 2020WPMFE9 is acknowledged. Open Access Funding provided by Universita degli Studi di Padova within the CRUI-CARE Agreement.

## References

Ai, H.-A., & Ahrens, T. J. (2004). Dynamic tensile strength of terrestrial rocks and application to impact cratering. *Meteoritics & Planetary Sciences*, *39*(2), 233–246. https://doi.org/10.1111/j.1945-5100.2004.tb00338.x

Altenberger, U., Prosser, G., Grande, A., Günter, C., & Langone, A. (2013). A seismogenic zone in the deep crust indicated by pseudotachylytes and ultramylonites in granulite-facies rocks of Calabria (Southern Italy). *Contributions to Mineralogy and Petrology*, *166*(4), 975–994. https://doi.org/10.1007/s00410-013-0904-3

Altenberger, U., Prosser, G., Ruggiero, M., & Günter, C. (2011). Microstructure and petrology of a Calabrian garnet-bearing pseudotachylyte—A link to lower-crustal seismicity. *Geological Society, London, Special Publications*, *359*(1), 153–168. https://doi.org/10.1144/sp359.9

Andersen, T., Austrheim, H., Burke, E. A. J., & Elvevold, S. (1993). $N_2$ and $CO_2$ in deep crustal fluids: Evidence from the Caledonides of Norway. *Chemical Geology*, *108*(1), 113–132. https://doi.org/10.1016/0009-2541(93)90320-I

Anderson, E. K., Song, W. J., Johnson, S. E., & Cruz-Uribe, A. M. (2021). Mica kink-band geometry as an indicator of coseismic dynamic loading. *Earth and Planetary Science Letters*, *567*, 117000. https://doi.org/10.1016/j.epsl.2021.117000

Andrews, D. J. (2005). Rupture dynamics with energy loss outside the slip zone. *Journal of Geophysical Research*, *110*(B1). https://doi.org/10.1029/2004JB003191

Aupart, C., Dunkel, K. G., Angheluta, L., Austrheim, H., Ildefonse, B., Malthe-Sørenssen, A., & Jamtveit, B. (2018). Olivine grain size distributions in faults and shear zones: Evidence for non steady state deformation. *Journal of Geophysical Research: Solid Earth*, *123*(9), 7421–7443. https://doi.org/10.1029/2018jb015836

Austrheim, H. (1987). Eclogitization of lower crustal granulites by fluid migration through shear zones. *Earth and Planetary Science Letters*, *81*(2–3), 221–232. https://doi.org/10.1016/0012-821X(87)90158-0

Austrheim, H., & Boundy, T. M. (1994). Pseudotachylytes generated during seismic faulting and eclogitization of the deep crust. *Science*, *265*, 82–83. https://doi.org/10.1126/science.265.5168.82

Austrheim, H., Dunkel, K. G., Plümper, O., Ildefonse, B., Liu, Y., & Jamtveit, B. (2017). Fragmentation of wall rock garnets during deep crustal earthquakes. *Science Advances*, *3*(2), e1602067. https://doi.org/10.1126/sciadv.1602067

Austrheim, H., & Engvik, A. K. (1997). Fluid transport, deformation and metamorphism at depth in a collision zone. In B. Jamtveit, & B. W. D. Yardley (Eds.), *Fluid flow and transport in rocks* (pp. 123–137). Chapman & Hall. https://doi.org/10.1007/978-94-009-1533-6_7

Austrheim, H., & Griffin, W. L. (1985). Shear deformation and eclogite formation within granulite-facies anorthosites of the Bergen Arcs, Western Norway. *Chemical Geology*, *50*(1), 267–281. https://doi.org/10.1016/0009-2541(85)90124-X

Bachmann, F., Hielscher, R., & Schaeben, H. (2010). Texture analysis with MTEX–Free and open source software toolbox. *Solid State Phenomena*, *160*, 63–68. https://doi.org/10.4028/www.scientific.net/SSP.160.63

Bargossi, G. M., Bondi, M., Landini, F., & Morten, L. (1982). Il plutone di Monte croce (Alto Adige, Nord Italia). *Rendiconti della Societa Italiana di Mineralogia e Petrologia*, *38*(1), 155–162.

Behera, B. M., Thirukumaran, V., Soni, A., Mishra, P. K., & Biswal, T. K. (2017). Size distribution and roundness of clasts within pseudotachylytes of the Gangavalli Shear Zone, Salem, Tamil Nadu: An insight into its origin and tectonic significance. *Journal of Earth System Science*, *126*(4). https://doi.org/10.1007/s12040-017-0827-x

Bell, T. H. (1979). The deformation and recrystallization of biotites in the Woodroffe Thrust mylonite zone. *Tectonophysics*, *58*, 139–158. https://doi.org/10.1016/0040-1951(79)90326-3

Bell, T. H., & Etheridge, M. A. (1976). The deformation and recrystallization of quartz in a mylonite zone. *Tectonophysics*, *32*, 235–267. https://doi.org/10.1016/0040-1951(76)90064-0

Bestmann, M., Pennacchioni, G., Frank, G., Goken, M., & de Wall, H. (2011). Pseudotachylyte in muscovite-bearing quartzite: Coseismic friction-induced melting and plastic deformation of quartz. *Journal of Structural Geology*, *33*(2), 169–186. https://doi.org/10.1016/j.jsg.2010.10.009

Bestmann, M., Pennacchioni, G., Mostefaoui, S., Goken, M., & de Wall, H. (2016). Instantaneous healing of micro-fractures during coseismic slip: Evidence from microstructure and Ti in quartz geochemistry within an exhumed pseudotachylyte-bearing fault in tonalite. *Lithos*, *254*, 84–93. https://doi.org/10.1016/j.lithos.2016.03.011

Bestmann, M., Pennacchioni, G., Nielsen, S., Goken, M., & de Wall, H. (2012). Deformation and ultrafine dynamic recrystallization of quartz in pseudotachylyte-bearing brittle faults: A matter of a few seconds. *Journal of Structural Geology*, *38*, 21–38. https://doi.org/10.1016/j.jsg.2011.10.001

Bizzarri, A. (2014). The destiny of a clast within a molten pseudotachylyte vein. *Bulletin of the Seismological Society of America*, *104*(5), 2399–2411. https://doi.org/10.1785/0120140084

Bjørnerud, M. (2010). Rethinking conditions necessary for pseudotachylyte formation: Observations from the Otago schists, South Island, New Zealand. *Tectonophysics*, *490*(1), 69–80. https://doi.org/10.1016/j.tecto.2010.04.028

Blenkinsop, T. G. (1991). Cataclasis and processes of particle size reduction. *Pure and Applied Geophysics*, *136*(1), 59–86. https://doi.org/10.1007/BF00878888

Boundy, T. M., Fountain, D. M., & Austrheim, H. (1992). Structural development and petrofabrics of eclogite facies shear zones, Bergen Arcs, Western Norway: Implications for deep crustal deformational processes. *Journal of Metamorphic Geology*, *10*(2), 127–146. https://doi.org/10.1111/j.1525-1314.1992.tb00075.x

Brace, W. F., & Martin, R. J. (1968). A test of the law of effective stress for crystalline rocks of low porosity. *International Journal of Rock Mechanics and Mining Sciences*, *5*(5), 415–426. https://doi.org/10.1016/0148-9062(68)90045-4

Brantut, N. (2020). Dilatancy-induced fluid pressure drop during dynamic rupture: Direct experimental evidence and consequences for earthquake dynamics. *Earth and Planetary Science Letters*, *538*, 116179. https://doi.org/10.1016/j.epsl.2020.116179

Buhl, E., Kowitz, A., Elbeshausen, D., Sommer, F., Dresen, G., Poelchau, M. H., et al. (2013). Particle size distribution and strain rate attenuation in hypervelocity impact and shock recovery experiments. *Journal of Structural Geology*, *56*, 20–33. https://doi.org/10.1016/j.jsg.2013.08.007

Bunge, H. J. (1982). *Texture analysis in materials science: Mathematical models*. Butterworths.

Camacho, A., Compston, W., McCulloch, M., & McDougall, I. (1997). Timing and exhumation of eclogite facies shear zones, Musgrave Block, central Australia. *Journal of Metamorphic Geology*, *15*(6), 735–751. https://doi.org/10.1111/j.1525-1314.1997.00053.x

Camacho, A., & McDougall, I. (2000). Intracratonic, strike-slip partitioned transpression and the formation and exhumation of eclogite facies rocks: An example from the Musgrave Block, central Australia. *Tectonics*, *19*(5), 978–996. https://doi.org/10.1029/1999TC001151

Camacho, A., Vernon, R. H., & Fitz Gerald, J. D. (1995). Large volumes of anhydrous pseudotachylyte in the Woodroffe thrust, eastern Musgrave ranges, Australia. *Journal of Structural Geology*, *17*(3), 371–383. https://doi.org/10.1016/0191-8141(94)00069-C

Camacho, A., Yang, P., & Frederiksen, A. (2009). Constraints from diffusion profiles on the duration of high-strain deformation in thickened crust. *Geology*, *37*(8), 755–758. https://doi.org/10.1130/g25753a.1

Chao, H. L., & Parker, T. E. (1983). 1–3 June 1983)Tensile fracture strength of ST cut quartz. *Symposium on Frequency Control*. Paper presented at the 37th Annual. https://doi.org/10.1109/FREQ.1983.200654

Cross, A. J., Prior, D. J., Stipp, M., & Kidder, S. (2017). The recrystallized grain size piezometer for quartz: An EBSD-based calibration. *Geophysical Research Letters*, *44*(13), 6667–6674. https://doi.org/10.1002/2017GL073836

Deb, T., Bhattacharyya, T., Matin, A., & Sensarma, S. (2015). Origin of pseudotachylytes based on clasts size frequency distribution in Bundelkhand Craton, Central India. *Journal of the Geological Society of India*, *85*(5), 551–556. https://doi.org/10.1007/s12594-015-0249-9

Di Toro, G., Nielsen, S., & Pennacchioni, G. (2005). Earthquake rupture dynamics frozen in exhumed ancient faults. *Nature*, *436*(7053), 1009–1012. https://doi.org/10.1038/nature03910

Di Toro, G., & Pennacchioni, G. (2004). Superheated friction-induced melts in zoned pseudotachylytes within the Adamello tonalites (Italian Southern Alps). *Journal of Structural Geology*, *26*(10), 1783–1801. https://doi.org/10.1016/j.jsg.2004.03.001

Di Toro, G., & Pennacchioni, G. (2005). Fault plane processes and mesoscopic structure of a strong-type seismogenic fault in tonalites (Adamello batholith, Southern Alps). *Tectonophysics*, *402*(1–4), 55–80. https://doi.org/10.1016/j.tecto.2004.12.036

Di Toro, G., Pennacchioni, G., & Nielsen, S. (2009). Pseudotachylytes and earthquake source mechanics. In *Fault-Zone Properties and Earthquake Rupture Dynamics*. In F. Eiichi (Ed.), (Vol. 94, pp. 87–133). Academic Press. https://doi.org/10.1016/s0074-6142(08)00005-3

Di Toro, G., Pennacchioni, G., & Teza, G. (2005). Can pseudotachylytes be used to infer earthquake source parameters? An example of limitations in the study of exhumed faults. *Tectonophysics*, *402*(1–4), 3–20. https://doi.org/10.1016/j.tecto.2004.10.014

Dunkel, K. G., Morales, L. F. G., & Jamtveit, B. (2021). Pristine microstructures in pseudotachylytes formed in dry lower crust, Lofoten, Norway. *Philosophical Transactions of the Royal Society A: Mathematical, Physical & Engineering Sciences*, *379*(2193), 20190423. https://doi.org/10.1098/rsta.2019.0423

Ellis, D. J., & Maboko, M. A. H. (1992). Precambrian tectonics and the physicochemical evolution of the continental crust. I. The gabbro-eclogite transition revisited. *Precambrian Research*, *55*(1), 491–506. https://doi.org/10.1016/0301-9268(92)90041-L

Fowler, A. C., & Scheu, B. (2016). A theoretical explanation of grain size distributions in explosive rock fragmentation. *Proceedings. Mathematical, physical, and engineering sciences*, *472*(2190), 20150843. https://doi.org/10.1098/rspa.2015.0843

Frank, F. C. (1965). On dilatancy in relation to seismic sources. *Reviews of Geophysics*, *3*(4), 485–503. https://doi.org/10.1029/RG003i004p00485

Frank, F. C. (1966). A further note on dilatancy in relation to seismic sources. *Reviews of Geophysics*, *4*(3), 405–408. https://doi.org/10.1029/RG004i003p00405

Handy, M. R., Hirth, G., & Bürgmann, R. (2007). Continental fault structure and rheology from the frictional-viscous transition downward. In M. R. Handy, G. Hirth, & N. Hovius (Eds.), *Tectonic faults—Agents of change on a dynamic Earth* (pp. 139–182). MIT Press.

Hawemann, F., Mancktelow, N., Wex, S., Pennacchioni, G., & Camacho, A. (2019). Fracturing and crystal plastic behaviour of garnet under seismic stress in the dry lower continental crust (Musgrave Ranges, Central Australia). *Solid Earth*, *10*(5), 1635–1649. https://doi.org/10.5194/se-10-1635-2019

Hawemann, F., Mancktelow, N. S., Pennacchioni, G., Wex, S., & Camacho, A. (2019). Weak and slow, strong and fast: How shear zones evolve in a dry continental crust (Musgrave Ranges, central Australia). *Journal of Geophysical Research: Solid Earth*, *124*(1), 219–240. https://doi.org/10.1029/2018jb016559

Hawemann, F., Mancktelow, N. S., Wex, S., Camacho, A., & Pennacchioni, G. (2018). Pseudotachylyte as field evidence for lower-crustal earthquakes during the intracontinental Petermann Orogeny (Musgrave block, central Australia). *Solid Earth*, *9*(3), 629–648. https://doi.org/10.5194/se-9-629-2018

Hayward, K. S., Cox, S. F., Fitz Gerald, J. D., Slagmolen, B. J. J., Shaddock, D. A., Forsyth, P. W. F., et al. (2016). Mechanical amorphization, flash heating, and frictional melting: Dramatic changes to fault surfaces during the first millisecond of earthquake slip. *Geology*, *44*(12), 1043–1046. https://doi.org/10.1130/g38242.1

Heilbronner, R., & Keulen, N. (2006). Grain size and grain shape analysis of fault rocks. *Tectonophysics*, *427*(1), 199–216. https://doi.org/10.1016/j.tecto.2006.05.020

Hentschel, F., Trepmann, C. A., & Janots, E. (2019). Deformation of feldspar at greenschist facies conditions – The record of mylonitic pegmatites from the Pfunderer Mountains, Eastern Alps. *Solid Earth*, *10*(1), 95–116. https://doi.org/10.5194/se-10-95-2019

Hielscher, R., & Schaeben, H. (2008). A novel pole figure inversion method: Specification of the MTEX algorithm. *Journal of Applied Crystallography*, *41*(6), 1024–1037. https://doi.org/10.1107/S0021889808030112

Hisada, E. (2004). Clast-size analysis of impact-generated pseudotachylite from Vredefort Dome, South Africa. *Journal of Structural Geology*, *26*(8), 1419–1424. https://doi.org/10.1016/j.jsg.2003.10.007

Incel, S., Schubnel, A., Renner, J., John, T., Labrousse, L., Hilairet, N., et al. (2019). Experimental evidence for wall-rock pulverization during dynamic rupture at ultra-high pressure conditions. *Earth and Planetary Science Letters*, *528*, 115832. https://doi.org/10.1016/j.epsl.2019.115832

Jamtveit, B., Ben-Zion, Y., Renard, F., & Austrheim, H. (2018). Earthquake-induced transformation of the lower crust. *Nature*, *556*(7702), 487–491. https://doi.org/10.1038/s41586-018-0045-y

Jamtveit, B., Bucher-Nurminen, K., & Austrheim, H. (1990). Fluid controlled eclogitization of granulites in deep crustal shear zones, Bergen arcs, Western Norway. *Contributions to Mineralogy and Petrology*, *104*(2), 184–193. journal article. https://doi.org/10.1007/bf00306442

Jamtveit, B., Moulas, E., Andersen, T. B., Austrheim, H., Corfu, F., Petley-Ragan, A., & Schmalholz, S. M. (2018). High pressure metamorphism caused by fluid induced weakening of deep continental crust. *Scientific Reports*, *8*(1), 17011. https://doi.org/10.1038/s41598-018-35200-1

Jamtveit, B., Petley-Ragan, A., Incel, S., Dunkel, K. G., Aupart, C., Austrheim, H., et al. (2019). The effects of earthquakes and fluids on the metamorphism of the lower continental crust. *Journal of Geophysical Research: Solid Earth*, *124*(8), 7725–7755. https://doi.org/10.1029/2018jb016461

John, T., Medvedev, S., Rupke, L. H., Andersen, T. B., Podladchikov, Y. Y., & Austrheim, H. (2009). Generation of intermediate-depth earthquakes by self-localizing thermal runaway. *Nature Geoscience*, *2*(2), 137–140. https://doi.org/10.1038/ngeo419

Kaatz, L., Zertani, S., Moulas, E., John, T., Labrousse, L., Schmalholz, S. M., & Andersen, T. B. (2021). Widening of hydrous shear zones during incipient eclogitization of metastable dry and rigid lower crust—Holsnøy, Western Norway. *Tectonics*, *40*(3), e2020TC006572. https://doi.org/10.1029/2020TC006572

Kavner, A. (2007). Garnet yield strength at high pressures and implications for upper mantle and transition zone rheology. *Journal of Geophysical Research*, *112*(B12). https://doi.org/10.1029/2007JB004931

Kelemen, P. B., & Hirth, G. (2007). A periodic shear-heating mechanism for intermediate-depth earthquakes in the mantle. *Nature*, *446*(7137), 787–790. https://doi.org/10.1038/nature05717

Kohlstedt, D. L., Evans, B., & Mackwell, S. J. (1995). Strength of the lithosphere: Constraints imposed by laboratory experiments. *Journal of Geophysical Research*, *100*(B9), 17587–17602. https://doi.org/10.1029/95jb01460

Larsen, R. B., Eide, E. A., & Burke, E. A. J. (1998). Evolution of metamorphic volatiles during exhumation of microdiamond-bearing granulites in the Western Gneiss Region, Norway. *Contributions to Mineralogy and Petrology*, *133*(1), 106–121. https://doi.org/10.1007/s004100050441

Lee, S. K., Han, R., Kim, E. J., Jeong, G. Y., Khim, H., & Hirose, T. (2017). Quasi-equilibrium melting of quartzite upon extreme friction. *Nature Geoscience*, *10*(6), 436–441. https://doi.org/10.1038/ngeo2951

Lin, A. M., Maruyama, T., Aaron, S., Michibayashi, K., Camacho, A., & Kano, K. I. (2005). Propagation of seismic slip from brittle to ductile crust: Evidence from pseudotachylyte of the Woodroffe thrust, central Australia. *Tectonophysics*, *402*(1–4), 21–35. https://doi.org/10.1016/j.tecto.2004.10.016

Lund, M. G., & Austrheim, H. (2003). High-pressure metamorphism and deep-crustal seismicity: Evidence from contemporaneous formation of pseudotachylytes and eclogite facies coronas. *Tectonophysics*, *372*(1–2), 59–83. https://doi.org/10.1016/s0040-1951(03)00232-4

Maddock, R. H. (1983). Melt origin of fault-generated pseudotachylytes demonstrated by textures. *Geology*, *11*(2), 105–108. https://doi.org/10.1130/0091-7613(1983)11<105:moofpd>2.0.co;2

Major, R. B. (1973). *Woodroffe, South Australia, 1:250000 geological series, explanatory notes*. Retrieved from South Australian Department of Mines and Energy. https://sarigbasis.pir.sa.gov.au/WebtopEw/ws/samref/sarig1/wcir/Record;jsessionid=ADAC8C872D78F1AAFBCADBAB6A20E83F

Mancktelow, N. S. (2008). Tectonic pressure: Theoretical concepts and modelled examples. *Lithos*, *103*(1–2), 149–177. https://doi.org/10.1016/j.lithos.2007.09.013

Mancktelow, N. S., & Pennacchioni, G. (2004). The influence of grain boundary fluids on the microstructure of quartz-feldspar mylonites. *Journal of Structural Geology*, *26*(1), 47–69. https://doi.org/10.1016/S0191-8141(03)00081-6

Menegon, L., Pennacchioni, G., Malaspina, N., Harris, K., & Wood, E. (2017). Earthquakes as precursors of ductile shear zones in the dry and strong lower crust. *Geochemistry, Geophysics, Geosystems*, *18*(12), 4356–4374. https://doi.org/10.1002/2017gc007189

Neikov, O. D., & Yefimov, N. A. (2019). Chapter 1–Powder characterization and testing. In O. D. Neikov, S. S. Naboychenko, & N. A. Yefimov (Eds.), *Handbook of non-ferrous metal powders* (2nd edn, pp. 3–62). Elsevier. https://doi.org/10.1016/B978-0-08-100543-9.00001-4

Niemeijer, A., Di Toro, G., Nielsen, S., & Di Felice, F. (2011). Frictional melting of gabbro under extreme experimental conditions of normal stress, acceleration, and sliding velocity. *Journal of Geophysical Research*, *116*(B7). https://doi.org/10.1029/2010JB008181

Okubo, K., Bhat, H. S., Rougier, E., Marty, S., Schubnel, A., Lei, Z., et al. (2019). Dynamics, radiation, and overall energy budget of earthquake rupture with coseismic off-fault damage. *Journal of Geophysical Research: Solid Earth*, *124*(11), 11771–11801. https://doi.org/10.1029/2019JB017304

Okudaira, T., Bando, H., & Yoshida, K. (2013). Grain-boundary diffusion rates inferred from grain-size variations of quartz in metacherts from a contact aureole. *American Mineralogist*, *98*(4), 680–688. https://doi.org/10.2138/am.2013.4308

Orlandini, O. F., & Mahan, K. H. (2020). Rheological evolution of a pseudotachylyte-bearing deep crustal shear zone in the Western Canadian shield. *Journal of Structural Geology*, *141*, 104188. https://doi.org/10.1016/j.jsg.2020.104188

Orlandini, O. F., Mahan, K. H., Williams, M. J., Regan, S. P., & Mueller, K. J. (2018). Evidence for deep crustal seismic rupture in a granulite-facies, intraplate, strike-slip shear zone, northern Saskatchewan, Canada. *The Geological Society of America Bulletin*, *131*(3–4), 403–425. https://doi.org/10.1130/b31922.1

Papa, S., Pennacchioni, G., Angel, R. J., & Faccenda, M. (2018). The fate of garnet during (deep-seated) coseismic frictional heating: The role of thermal shock. *Geology*, *46*(5), 471–474. https://doi.org/10.1130/g40077.1

Papa, S., Pennacchioni, G., Menegon, L., & Thielmann, M. (2020). High-stress creep preceding coseismic rupturing in amphibolite-facies ultramylonites. *Earth and Planetary Science Letters*, *541*, 116260. https://doi.org/10.1016/j.epsl.2020.116260

Papa, S., Spagnuolo, E., Di Toro, G., Cavallo, A., Favero, M., Camacho, A., & Pennacchioni, G. (2021). Selective clast survival in an experimentally-produced pseudotachylyte. *Journal of Structural Geology*, *147*, 104328. https://doi.org/10.1016/j.jsg.2021.104328

Pardavi-Horváth, M. (1984). Microhardness and brittle fracture of garnet single crystals. *Journal of Materials Science*, *19*(4), 1159–1170. https://doi.org/10.1007/BF01120025

Passchier, C. W. (1982). Pseudotachylyte and the development of ultramylonite bands in the Saint-Barthelemy massif, French Pyrenees. *Journal of Structural Geology*, *4*(1), 69–79. https://doi.org/10.1016/0191-8141(82)90008-6

Paterson, M. S. (1978). *Experimental rock deformation. The brittle field*. Springer Verlag.

Pennacchioni, G., Scambelluri, M., Bestmann, M., Notini, L., Nimis, P., Plümper, O., et al. (2020). Record of intermediate-depth subduction seismicity in a dry slab from an exhumed ophiolite. *Earth and Planetary Science Letters*, *548*, 116490. https://doi.org/10.1016/j.epsl.2020.116490

Petley-Ragan, A., Ben-Zion, Y., Austrheim, H., Ildefonse, B., Renard, F., & Jamtveit, B. (2019). Dynamic earthquake rupture in the lower crust. *Science Advances*, *5*(7), eaaw0913. https://doi.org/10.1126/sciadv.aaw0913

Petley-Ragan, A., Dunkel, K. G., Austrheim, H., Ildefonse, B., & Jamtveit, B. (2018). Microstructural records of earthquakes in the lower crust and associated fluid-driven metamorphism in plagioclase-rich granulites. *Journal of Geophysical Research: Solid Earth*, *123*(5), 3729–3746. https://doi.org/10.1029/2017JB015348

Petley-Ragan, A. J., Plümper, O., Ildefonse, B., & Jamtveit, B. (2021). Nanoscale earthquake records preserved in plagioclase microfractures from the lower continental crust. *Solid Earth*, *12*(4), 959–969. https://doi.org/10.5194/se-12-959-2021

Phillips, N. J., & Williams, R. T. (2021). To D or not to D? Re-evaluating particle-size distributions in natural and experimental fault rocks. *Earth and Planetary Science Letters*, *553*, 116635. https://doi.org/10.1016/j.epsl.2020.116635

Pittarello, L., Di Toro, G., Bizzarri, A., Pennacchioni, G., Hadizadeh, J., & Cocco, M. (2008). Energy partitioning during seismic slip in pseudotachylyte-bearing faults (Gole Large Fault, Adamello, Italy). *Earth and Planetary Science Letters*, *269*(1–2), 131–139. https://doi.org/10.1016/j.epsl.2008.01.052

Pittarello, L., Habler, G., Abart, R., & Rhede, D. (2015). Garnet growth in frictional melts of the Ivrea Zone (Italy). *Italian Journal of Geosciences*, *134*(1), 149–161. https://doi.org/10.3301/ijg.2014.53

Pittarello, L., Pennacchioni, G., & Di Toro, G. (2012). Amphibolite-facies pseudotachylytes in Premosello metagabbro and felsic mylonites (Ivrea Zone, Italy). *Tectonophysics*, *580*, 43–57. https://doi.org/10.1016/j.tecto.2012.08.001

Price, N. J., & Cosgrove, J. W. (1990). *Analysis of geological structures*. Cambridge University Press.

Reches, Z., & Dewers, T. A. (2005). Gouge formation by dynamic pulverization during earthquake rupture. *Earth and Planetary Science Letters*, *235*(1), 361–374. https://doi.org/10.1016/j.epsl.2005.04.009

Rice, J. R., Sammis, C. G., & Parsons, R. (2005). Off-fault secondary failure induced by a dynamic slip pulse. *Bulletin of the Seismological Society of America*, *95*(1), 109–134. https://doi.org/10.1785/0120030166

Sammis, C. G., Osborne, R. H., Anderson, J. L., Banerdt, M., & White, P. (1986). Self-similar cataclasis in the formation of fault gouge. *Pure and Applied Geophysics*, *124*(1), 53–78. https://doi.org/10.1007/BF00875719

Sarkar, A., Bhattacharjee, D., & Chattopadhyay, A. (2020). Size distribution of survivor clasts in pseudotachylyte and cataclasite: Implications for crushing and melting processes in seismic fault zones. *Journal of Earth System Science*, *129*(1), 216. https://doi.org/10.1007/s12040-020-01480-3

Sarkar, A., Chattopadhyay, A., & Singh, T. (2019). Roundness of survivor clasts as a discriminator for melting and crushing origin of fault rocks: A reappraisal. *Journal of Earth System Science*, *128*(3), 51. https://doi.org/10.1007/s12040-019-1072-2

Sibson, R. H. (1975). Generation of pseudotachylite by ancient seismic faulting. *Geophysical Journal of the Royal Astronomical Society*, *43*, 775–794. https://doi.org/10.1111/j.1365-246X.1975.tb06195.x

Sibson, R. H. (1977). Fault rocks and fault mechanisms. *Journal of the Geological Society*, *133*, 191–213. https://doi.org/10.1144/gsjgs.133.3.0191

Sibson, R. H. (1980). Transient discontinuities in ductile shear zones. *Journal of Structural Geology*, *2*(1–2), 165–171. https://doi.org/10.1016/0191-8141(80)90047-4

Sibson, R. H. (1982). Fault zone models, heat flow, and the depth distribution of earthquakes in the continental crust of the United States. *Bulletin of the Seismological Society of America*, *72*(1), 151–163. https://doi.org/10.1785/BSSA0720010151

Sibson, R. H., & Toy, V. G. (2006). The habitat of fault-generated pseudotachylyte: Presence vs. absence of friction-melt *Earthquakes: Radiated energy and the physics of faulting* (Vol. 170, pp. 153–166). AGU. https://doi.org/10.1029/170gm16

Skemer, P., Katayama, I., Jiang, Z., & Karato, S. (2005). The misorientation index: Development of a new method for calculating the strength of lattice-preferred orientation. *Tectonophysics*, *411*(1), 157–167. https://doi.org/10.1016/j.tecto.2005.08.023

Song, B. R., Johnson, S. E., Song, W. J., Gerbi, C. C., & Yates, M. G. (2020). Coseismic damage runs deep in continental strike-slip faults. *Earth and Planetary Science Letters*, *539*, 116226. https://doi.org/10.1016/j.epsl.2020.116226

Song, S. J., Choo, C. O., Chang, C. J., & Jang, Y. D. (2017). A microstructural study of the fault gouge in the granite, Yangbuk, Gyeongju, southeastern Korea, with implications for multiple faulting. *Geosciences Journal*, *21*(1), 1–19. https://doi.org/10.1007/s12303-016-0021-1

Spray, J. G. (1992). A physical basis for the frictional melting of some rock-forming minerals. *Tectonophysics*, *204*(3–4), 205–221. https://doi.org/10.1016/0040-1951(92)90308-s

Spray, J. G. (2010). Frictional melting processes in planetary materials: From hypervelocity impact to earthquakes. *Annual Review of Earth and Planetary Sciences*, *38*, 221–254. https://doi.org/10.1146/annurev.earth.031208.100045

Steltenpohl, M. G., Kassos, G., & Andresen, A. (2006). Retrograded eclogite-facies pseudotachylytes as deep-crustal paleoseismic faults within continental basement of Lofoten, North Norway. *Geosphere*, *2*(1), 61–72. https://doi.org/10.1130/ges00035.1

Suzuki, T. (2012). Understanding of dynamic earthquake slip behavior using damage as a tensor variable: Microcrack distribution, orientation, and mode and secondary faulting. *Journal of Geophysical Research*, *117*(B5). https://doi.org/10.1029/2011jb008908

Swanson, M. T. (1992). Fault structure, wear mechanisms and rupture processes in pseudotachylyte generation. *Tectonophysics*, *204*(3–4), 223–242. https://doi.org/10.1016/0040-1951(92)90309-T

Tasaka, M., Zimmerman, M. E., & Kohlstedt, D. L. (2016). Evolution of the rheological and microstructural properties of olivine aggregates during dislocation creep under hydrous conditions. *Journal of Geophysical Research: Solid Earth*, *121*(1), 92–113. https://doi.org/10.1002/2015JB012134

Thielmann, M. (2018). Grain size assisted thermal runaway as a nucleation mechanism for continental mantle earthquakes: Impact of complex rheologies. *Tectonophysics*, *746*, 611–623. https://doi.org/10.1016/j.tecto.2017.08.038

Thielmann, M., Rozel, A., Kaus, B. J. P., & Ricard, Y. (2015). Intermediate-depth earthquake generation and shear zone formation caused by grain size reduction and shear heating. *Geology*, *43*(9), 791–794. https://doi.org/10.1130/g36864.1

Trepmann, C. A., Hsu, C., Hentschel, F., Döhler, K., Schneider, C., & Wichmann, V. (2017). Recrystallization of quartz after low-temperature plasticity – the record of stress relaxation below the seismogenic zone. *Journal of Structural Geology*, *95*, 77–92. https://doi.org/10.1016/j.jsg.2016.12.004

Trepmann, C. A., & Stockhert, B. (2002). Cataclastic deformation of garnet: A record of synseismic loading and postseismic creep. *Journal of Structural Geology*, *24*(11), 1845–1856. https://doi.org/10.1016/S0191-8141(02)00004-4

Trepmann, C. A., Stöckhert, B., Dorner, D., Moghadam, R. H., Küster, M., & Röller, K. (2007). Simulating coseismic deformation of quartz in the middle crust and fabric evolution during postseismic stress relaxation—An experimental study. *Tectonophysics*, *442*(1), 83–104. https://doi.org/10.1016/j.tecto.2007.05.005

Turcotte, D. L. (1986). Fractals and fragmentation. *Journal of Geophysical Research*, *91*(B2), 1921–1926. https://doi.org/10.1029/JB091iB02p01921

Walsh, A. K., Kelsey, D. E., Kirkland, C. L., Hand, M., Smithies, R. H., Clark, C., & Howard, H. M. (2015). P–T–t evolution of a large, long-lived, ultrahigh-temperature Grenvillian belt in central Australia. *Gondwana Research*, *28*(2), 531–564. https://doi.org/10.1016/j.gr.2014.05.012

Wenk, H. R., & Weiss, L. E. (1982). Al-rich calcic pyroxene in pseudotachylite: An indicator of high pressure and high temperature? *Tectonophysics*, *84*(2–4), 329–341. https://doi.org/10.1016/0040-1951(82)90166-4

Wex, S., Mancktelow, N. S., Camacho, A., & Pennacchioni, G. (2019). Interplay between seismic fracture and aseismic creep in the Woodroffe Thrust, central Australia—Inferences for the rheology of relatively dry continental mid-crustal levels. *Tectonophysics*, *758*, 55–72. https://doi.org/10.1016/j.tecto.2018.10.024

Wex, S., Mancktelow, N. S., Hawemann, F., Camacho, A., & Pennacchioni, G. (2017). Geometry of a large-scale, low-angle, midcrustal thrust (Woodroffe Thrust, central Australia). *Tectonics*, *36*(11), 2447–2476. https://doi.org/10.1002/2017tc004681

Wex, S., Mancktelow, N. S., Hawemann, F., Camacho, A., & Pennacchioni, G. (2018). Inverted distribution of ductile deformation in the relatively "dry" middle crust across the Woodroffe Thrust, central Australia. *Solid Earth*, *9*(4), 859–878. https://doi.org/10.5194/se-9-859-2018

White, J. C. (1996). Transient discontinuities revisited: Pseudotachylyte, plastic instability and the influence of low pore fluid pressure on deformation processes in the mid-crust. *Journal of Structural Geology*, *18*(12), 1471–1477. https://doi.org/10.1016/S0191-8141(96)00059-4

Wilson, B., Dewers, T., Reches, Z. e., & Brune, J. (2005). Particle size and energetics of gouge from earthquake rupture zones. *Nature*, *434*, 749. https://doi.org/10.1038/nature03433

Wright, S. I., & Nowell, M. M. (2006). EBSD image quality mapping. *Microscopy and Microanalysis*, *12*(1), 72–84. https://doi.org/10.1017/S1431927606060090

Wright, S. I., Nowell, M. M., & Field, D. P. (2011). A review of strain analysis using electron backscatter diffraction. *Microscopy and Microanalysis*, *17*(3), 316–329. https://doi.org/10.1017/S1431927611000055

Yamashita, T. (2000). Generation of microcracks by dynamic shear rupture and its effects on rupture growth and elastic wave radiation. *Geophysical Journal International*, *143*(2), 395–406. https://doi.org/10.1046/j.1365-246X.2000.01238.x

Zhong, X., Petley-Ragan, A. J., Incel, S. H. M., Dabrowski, M., Andersen, N. H., & Jamtveit, B. (2021). Lower crustal earthquake associated with highly pressurized frictional melts. *Nature Geoscience*, *14*(7), 519–525. https://doi.org/10.1038/s41561-021-00760-x

## References From the Supporting Information

Bachmann, F., Hielscher, R., & Schaeben, H. (2010). Texture analysis with MTEX - Free and open source software toolbox. *Solid State Phenomena*, *160*, 63–68. https://doi.org/10.4028/www.scientific.net/SSP.160.63

Bestmann, M., Pennacchioni, G., Nielsen, S., Goken, M., & de Wall, H. (2012). Deformation and ultrafine dynamic recrystallization of quartz in pseudotachylyte-bearing brittle faults: A matter of a few seconds. *Journal of Structural Geology*, *38*, 21–38. https://doi.org/10.1016/j.jsg.2011.10.001

Bunge, H. J. (1982). *Texture analysis in materials science: Mathematical models*. Butterworths.

Camacho, A., Vernon, R. H., & Fitz Gerald, J. D. (1995). Large volumes of anhydrous pseudotachylyte in the Woodroffe thrust, eastern Musgrave ranges, Australia. *Journal of Structural Geology*, *17*(3), 371–383. https://doi.org/10.1016/0191-8141(94)00069-C

Cross, A. J., Prior, D. J., Stipp, M., & Kidder, S. (2017). The recrystallized grain size piezometer for quartz: An EBSD-based calibration. *Geophysical Research Letters*, *44*(13), 6667–6674. https://doi.org/10.1002/2017GL073836

Hielscher, R., & Schaeben, H. (2008). A novel pole figure inversion method: Specification of the MTEX algorithm. *Journal of Applied Crystallography*, *41*(6), 1024–1037. https://doi.org/10.1107/S0021889808030112

Menegon, L., Pennacchioni, G., & Spiess, R. (2008). Dissolution-precipitation creep of K-feldspar in mid-crustal granite mylonites. *Journal of Structural Geology*, *30*(5), 565–579. https://doi.org/10.1016/j.jsg.2008.02.001

Skemer, P., Katayama, I., Jiang, Z., & Karato, S.-i. (2005). The misorientation index: Development of a new method for calculating the strength of lattice-preferred orientation. *Tectonophysics*, *411*(1), 157–167. https://doi.org/10.1016/j.tecto.2005.08.023

Trepmann, C. A., Hsu, C., Hentschel, F., Döhler, K., Schneider, C., & Wichmann, V. (2017). Recrystallization of quartz after low-temperature plasticity – the record of stress relaxation below the seismogenic zone. *Journal of Structural Geology*, *95*, 77–92. https://doi.org/10.1016/j.jsg.2016.12.004

Wex, S., Mancktelow, N. S., Camacho, A., & Pennacchioni, G. (2019). Interplay between seismic fracture and aseismic creep in the Woodroffe Thrust, central Australia – Inferences for the rheology of relatively dry continental mid-crustal levels. *Tectonophysics*, *758*, 55–72. https://doi.org/10.1016/j.tecto.2018.10.024